



**Calibration data for simultaneous determination of
P-V-X properties of binary and ternary CO₂ - CH₄ - N₂
gas mixtures by Raman spectroscopy over 5–600 bar:
Application to natural fluid inclusions**

Van-Hoan Le, Marie-Camille Caumon, Alexandre Tarantola, Aurelien Randi,
Pascal Robert, Josef Mullis

► **To cite this version:**

Van-Hoan Le, Marie-Camille Caumon, Alexandre Tarantola, Aurelien Randi, Pascal Robert, et al.. Calibration data for simultaneous determination of P-V-X properties of binary and ternary CO₂ - CH₄ - N₂ gas mixtures by Raman spectroscopy over 5–600 bar: Application to natural fluid inclusions. Chemical Geology, 2020, 552, pp.119783. 10.1016/j.chemgeo.2020.119783 . hal-02904254

HAL Id: hal-02904254

<https://hal.science/hal-02904254>

Submitted on 22 Aug 2022

HAL is a multi-disciplinary open access archive for the deposit and dissemination of scientific research documents, whether they are published or not. The documents may come from teaching and research institutions in France or abroad, or from public or private research centers.

L'archive ouverte pluridisciplinaire **HAL**, est destinée au dépôt et à la diffusion de documents scientifiques de niveau recherche, publiés ou non, émanant des établissements d'enseignement et de recherche français ou étrangers, des laboratoires publics ou privés.



Distributed under a Creative Commons Attribution - NonCommercial 4.0 International License

Calibration data for simultaneous determination of P - V - X properties of binary and ternary CO_2 - CH_4 - N_2 gas mixtures by Raman spectroscopy over 5-600 bar: Application to natural fluid inclusions

Van-Hoan Le ^{a,*}, Marie-Camille Caumon ^a, Alexandre Tarantola ^a, Aurélien Randi ^a, Pascal Robert ^a and Josef Mullis ^b

^a *Université de Lorraine, CNRS, GeoReSSources Laboratory, BP 70239, F-54506 Vandoeuvre-lès-Nancy, France*

^b *Department of Environmental Sciences, University of Basel, Bernoullistrasse 32, 4056, Basel, Switzerland*

* Corresponding author: van-hoan.le@univ-lorraine.fr

Abstract

The P - V - X properties of two-component fluid inclusions (FIs) are generally determined from microthermometry data using appropriate thermodynamic models (i.e., VX diagrams) and/or equations of state (EoS). However, some limitations can hamper the applicability of this technique such as the small size, low density or complex composition of the analyzed FI. Raman spectroscopy is known as the best-suited alternative method to microthermometry for the investigation of natural FIs because it can provide simultaneously non-destructive qualitative and possible quantitative analyses after specific calibrations. The present work aims to provide calibration data to directly determine the P - V - X properties of binary or ternary mixtures of CH_4 , CO_2 , and N_2 . The variation of spectral features as a function of composition and pressure (or density) was investigated by using Raman spectroscopy coupled with an improved High-Pressure Optical Cell (HPOC) system and a customized heating-cooling stage. From our experimental data, the relative Raman scattering cross-section (RRSCS) of CH_4 ($v_{\text{CH}_4}^*$) was demonstrated to be constant at 7.73 ± 0.16 over the investigated range of pressure (5-600 bars) and for any composition. This parameter can thus be used for the determination of composition with an uncertainty of ~ 0.5 mol%. Several calibration equations were calculated for different PX domains, linking the Fermi diad splitting of CO_2 (Δ) or the relative variation of the CH_4 peak position ($v_{\text{CH}_4}^*$) to the pressure (or density) and composition of CO_2 - CH_4 , CH_4 - N_2 , and CO_2 - N_2 - CH_4 mixtures at 22 and 32 °C. The pressure and density of the fluids can henceforth be directly measured from Raman spectra with an uncertainty of ~ 20 bars and $\sim 0.01 \text{ g}\cdot\text{cm}^{-3}$, respectively. Our calibration equations were then validated on natural FIs by comparing the results obtained from Raman and microthermometry. We also interpreted the variation of the peak position of CH_4 based on the change of intermolecular interaction. Finally, we discussed the applicability of the obtained calibration data into another laboratory by comparing it with the data of pure CO_2 and CH_4 published in literature. A small shift between calibration curves implies a systematic error which is perhaps due to the difference in the configuration or the day-to-day deviation of the instruments. Therefore, standards of well-known P - V - X properties should be regularly measured to prevent and to correct any variation or shifting of the instrumental responses.

Keywords: *Raman spectroscopy, gas mixtures, densimeter, barometer, high-pressure optical cell system, CO_2 Fermi diad splitting, fluid inclusions.*

1. Introduction

Geological fluids containing water (\pm salt) and gases are the essential vectors of heat and matter within the Earth's crust and mantle (Poty, 1967; Fyfe et al., 1978; Etheridge et al., 1983; Thompson and Connolly, 1992). CO_2 , CH_4 , and N_2 are the most common gaseous species omnipresent in various geological environments such as sedimentary basins (Benson and Cole, 2008; Fall et al., 2012; Lammers et al., 2015; Huang et al., 2018), diagenetic, low- and high-grade metamorphic rocks (Poty et al., 1974; Hollister and Burruss, 1976; Mullis, 1979; Frey et al., 1980; Mullis, 1987; Van den Kerkhof, 1988; Mullis et al., 1994; Touret, 2001; Van den Kerkhof and Thiéry, 2001; Tarantola et al., 2007), igneous rocks (Seitz et al., 1993), hydrothermal vent fluids at near mid-ocean ridges (Kelley, 1996; Charlou et al., 2002), and hydrothermal ore deposits (Roedder, 1979; Roedder and Bodnar, 1997; Diamond, 1990; Wilkinson, 2001; Bodnar et al., 2014). Natural fluid inclusions (FIs) are micro-volumes of geological fluids trapped within minerals during or after crystal growth. Thereby, they are assumed to preserve the P - T conditions of paleo-fluid circulations, so, become the most reliable samples of actual ancient geologic fluids. Investigating FIs is, therefore, an unavoidable step to get that useful information for the reconstruction of P - T history and the interpretation of different geological processes such as the source conditions, the mechanisms of mass and heat transportation involved in the precipitation and crystallization of rocks and host minerals, etc. (cf. reviews by Roedder, 1984 and Chi et al., 2003).

Microthermometry, a method based on the observation of phase transition temperatures, is currently the standard non-destructive method used for the investigation of fluid inclusions. The molar volume of one-component inclusions (i.e. pure CO_2 , CH_4 , or N_2) can be directly derived from the homogenization temperature using either empirical thermodynamic models or a proper equation of state (EoS) (Angus et al., 1976, 1979; Schneider, 1979; Duschek et al., 1990; Wagner and Pruss, 1993; Thiéry et al., 1994; Bakker and Diamond, 2000; Van den Kerkhof and Thiéry, 2001; Akinfiev and Diamond, 2010).

Regarding carbonic inclusions of binary systems, the Gibb's phase rule implies that one more phase transition temperature is required for the determination of both molar fraction (X) and molar volume (V). Several thermodynamic models were dedicatedly established for CO_2 - N_2 and CH_4 - CO_2 gas mixtures to directly infer the VX properties from the melting temperature $T_m(\text{vol})$ and homogenization temperature $T_h(\text{vol})$ of the volatile carbonic phase (Burruss, 1981; van den Kerkhof, 1990; Thiéry et al., 1994). Refined from the previously published models, the VX diagrams of Thiéry et al. (1994) are known as the most accurate and practical ones available in literature. However, the disadvantage of these models is that Thiéry et al. (1994) used two EoS, namely Soave (1972) to reproduce P - T - X values for liquid-vapor (LV) equilibria, and Lee and Kesler (1975) for density calculation, that may cause an incoherency of various fluid parameters (Bakker and Diamond, 2000). Using VX diagram of Thiéry et al. (1994), the uncertainties on measured composition and density arising from the error of

$T_m(\text{vol})$ and $T_h(\text{vol})$ ($\sim \pm 0.1$ °C) could reach up to ± 5 mol% and ± 0.09 g·cm⁻³, respectively, depending on VX domains (Le et al., 2019).

Otherwise, the VX properties of fluid inclusions could not be obtained by only using microthermometry, but must be combined with Raman spectroscopy, in the following cases:

- (i) Since the temperatures of the triple points of pure CO₂, CH₄, and N₂ are -56.6, -182.5 and -210 °C, respectively, mixing CO₂ with either CH₄ or N₂ will accordingly lower the $T_m(\text{vol})$. Thus, in the cases of CO₂-rich FIs (>80 mol% CO₂), the $T_m(\text{vol})$ obtained by microthermometry can be only used for checking the purity of CO₂ (Van den Kerkhof and Thiéry, 2001), and not for distinguishing between CO₂-CH₄ or CO₂-N₂ mixtures. Therefore, an additional Raman qualitative analysis is needed to confirm the actual composition of the binary system for choosing the appropriate VX diagram.
- (ii) The binary (CH₄-N₂) and ternary (CO₂-CH₄-N₂) mixtures are rare in nature but were also recognized in different geological settings (Van den Kerkhof, 1988; Noronha et al., 1992; Mullis et al., 1994; Cathelineau et al., 2017; Caumon et al., 2019). Since the melting temperature of CH₄-N₂ mixtures is normally unreachable (under -182.5 °C) with conventional microthermometry (cooling by liquid nitrogen), only the homogenization temperature occurring below -82.6 °C is observable, insufficient for the direct determination of VX properties. Microthermometry analyses of the ternary CO₂-CH₄-N₂ mixtures are also somewhat limited due to the complex phase behavior (Van den Kerkhof, 1988; Hurai et al., 2015). To the best of our knowledge, there was no available experimental diagram for the direct determination of *P-V-X* properties from microthermometry measurements only. Therefore, the composition of such systems (binary CH₄-N₂ and ternary CO₂-CH₄-N₂), in many cases, must be separately determined from Raman measurement (Hurai et al., 2015, p. 97), then coupled with microthermometry data and an EoS for further determination of density and or pressure.
- (iii) Gas hydrate phase can be formed during cooling-heating microthermometric experiments of high CO₂- (or CH₄-) bearing FIs and may remain above the homogenization of the volatile part of FI ($T_h(\text{vol})$), or ice melting temperature ($T_m(\text{ice})$) which, in turn, may affect the measured density (or salinity) deduced from $T_h(\text{vol})$ (or $T_m(\text{ice})$) only (Mullis, 1975, 1979; Collins, 1979; Diamond, 1992; Fall et al., 2011). This problem can be solved by using $T_h(\text{vol})$ and the final clathrate melting temperature $T_m(\text{cla})$ (DENSITY computer program by Bakker, 1997) (Diamond, 1994). However, one of the prerequisites of this program is the molar fraction of CO₂ and/or CH₄ and/or N₂ in the homogeneous carbonic phase. That means, once again, an additional Raman quantitative analysis is needed to be combined with microthermometry data.

Other limitations of microthermometry also appear when analyzing FIs of small size ($<5\text{ }\mu\text{m}$), of low density, and of even more complex composition without any observable phase transition (Rosso and Bodnar, 1995; Burke, 2001; Yamamoto et al., 2002; Kawakami et al., 2003; Yamamoto et al., 2007; Song et al., 2009).

Raman spectroscopy has been used since the 1970s for the study of natural fluid inclusions as a complementary method to microthermometry in different circumstances (as described above, and cf. review by Burke, 2001, Frezzotti et al., 2012, and Dubessy et al., 2012). It can offer fast (from a few seconds to a few minutes), high resolution ($\sim 1\text{ }\mu\text{m}^2$), and simultaneous non-destructive, multi-gases qualitative and quantitative analyses.

Generally, the molar fraction of gases can be measured from their peak areas if the Raman scattering cross-sections relative to that of N_2 (RRSCS) are known accurately. The review by Schrötter and Klöckner (1979) collected the RRSCSs of the most relevant gases in geological fluids and provided a detailed discussion about the dependence of this parameter. Indeed, the temperature and wavenumber dependence of RRSCS is minimal ($<1\%$) and can be negligible (Schrötter and Klöckner, 1979). However, the pressure and composition dependence of RRSCS is still questionable (Wopenka and Pasteris, 1986; Dubessy et al., 1989; Chou et al., 1990; Seitz et al., 1993, 1996). Indeed, every published RRSCS values were obtained on pure gases at low pressure ($1\text{--}5\text{ bars}$) and room temperature with an uncertainty varying from 5 to 20% and never reevaluated again (Burke, 2001), whereas natural FIs contain in many cases a gas mixture at elevated pressure. Using these old data may lead to considerable errors. Le et al. (2019) reevaluated the variation of RRSCS of two CO_2 bands and concluded that there is no correlation with the variation of the composition, but the RRSCS of the upper band (and lower band) slightly increased (and decreased) as pressure increased. Although the variation of the RRSCS of CO_2 with pressure can be negligible over 5–600 bars, it is still worth to check the variation of RRSCS of CH_4 over this PT range, especially because the RRSCS of CH_4 (~ 7.7) is much greater than that of CO_2 (≤ 1.4).

Not only providing the molar fraction, Raman spectra also reflect the interactions between the incident photons and the vibrational energy (frequency) of gaseous particles which are affected by intermolecular interactions and internal field (e.g., attractive or repulsive forces by surrounding molecules, electrostatic potential, polarization energy change, etc.). Therefore, the peak position of the Raman spectrum is literally related to the density (or pressure) of pure gases and gas mixtures. Raman spectroscopy appears then to be the best-suited technique for the study of the volatile part of natural FIs, yielding simultaneously P - V - X properties from Raman measurement only. Aiming to develop another alternative way for FI investigation, several applications of Raman spectroscopy were carried out (cf. review by Burke, 2001, and Frezzotti et al., 2012). Several calibration data were published for single-component gases that showed the variation of the peak position, and Fermi diad splitting of CO_2 as a function of pressure (density) and/or temperature: N_2 (Wang and Wright, 1973; Fabre and

Oksengorn, 1992; Lamadrid et al., 2018), CH₄ (Fabre and Oksengorn, 1992; Lin et al., 2007; Lu et al., 2007; Caumon et al., 2014; Zhang et al., 2016; Lamadrid et al., 2018), and CO₂ (Wright and Wang, 1973; Garrabos et al., 1980, 1989; Rosso and Bodnar, 1995; Kawakami et al., 2003; Yamamoto and Kagi, 2006; Wang et al., 2011; Fall et al., 2011; Yuan et al., 2017; Lamadrid et al., 2017; Wang et al., 2019). It is to note that these calibrations were made only for the cases of a pure component.

The effect of composition on the variation of the spectral features of CO₂, CH₄, and N₂ was reported very early by analyzing a binary (Fabre and Oksengorn, 1992; Hacura, 1997) or a ternary mixture (Lamadrid et al., 2018). However, there is a paucity of accurate experimental data covering a full composition-range of binary CO₂–CH₄–N₂ subsystems. For instance, the relationship between the Raman spectral features (peak shape, width, peak area/intensity ratio, peak position, etc.), the pressure (or density), and the composition of CO₂–CH₄ and CH₄–N₂ binary mixtures were revealed by Seitz et al. (1993, 1996). However, the results were somewhat scattered due to the use of low spectral resolution (~5 cm⁻¹). Besides, although Fermi diad splitting (Δ) is much more reliable with good reproducibility, Seitz et al. (1996) did not study the variation of Δ but study that of a single peak of CO₂ (ν^+ and ν^-) with the variation of the composition of CO₂–CH₄ mixtures. Consequently, no robust calibration with uncertainty analysis was given. Otherwise, the calibration data of CH₄–H₂ and CO₂–N₂ mixtures were recently provided by Fang et al. (2018) and Le et al. (2019), respectively, showing the capability of Raman spectroscopy to provide high-accurate quantitative analyses applicable for FI investigations. Furthermore, no calibration data for the CO₂–CH₄–N₂ ternary system by Raman spectroscopy is available yet in literature.

The present study aims (1) to redefine the RRSCS of the ν_1 band of CH₄ with considering the effect of composition and pressure, and (2) to establish Raman calibration data for binary and ternary mixtures of CO₂, CH₄, and N₂. For these purposes, Raman in-situ analyses of gas mixtures of known composition were performed at 22 and 32 °C (above the critical temperature of CO₂) over a pressure range from 5 to 600 bars thanks to an improved High-Pressure Optical Cell (HPOC) system coupled with a heating-cooling stage and a fused silica micro-capillary. The variations as a function of pressure and composition of the most reliable spectral parameters of each gas (Δ for CO₂, and peak position of the ν_1 band for CH₄) were thereby studied to provide the best-fitted regression calibration equations for the direct determination of *P-V-X* properties from Raman spectra. The latter were then applied to natural fluid inclusions hosted in quartz from the Central Alps, Switzerland (Mullis et al., 1994) and then compared with results from microthermometry for validation. Uncertainty analyses and applicability of our calibration were then discussed through a comparison with calibration data recently published in literature.

2. Material and Methods

The experimental protocol of the present study is similar to the one developed in our previous works (Le et al., 2019). It consists of three main steps (gas mixtures preparation, pressurization, in-situ

Raman analyses and data processing – Fig. A.1 in Appendix A) that are detailed in the following subsections.

2.1 Preparation of binary and ternary gas mixtures

Binary and ternary gas mixtures of desired compositions were prepared from high-purity CO₂, CH₄, and N₂ (99.99 % purity, Air LiquideTM) using a gas mixer (GasMix AlyTechTM). They were subsequently compressed up to ~130 bars and stored in a stainless-steel cylinder by a home-made compressor system. After the pressurization step, a gas chromatograph previously calibrated with different commercially standard mixtures of known compositions (purchased from Air LiquideTM) was used to double-check the actual composition of the prepared gas mixtures. The final composition of the gas mixtures is given with uncertainty of $\sim\pm 0.3$ mol% (1 σ). In this study, the CH₄-N₂ and CO₂-CH₄ binary mixtures were constituted by ~10, 20, 30, 50, 60, 70, 80 and 90 mol% CH₄; the CO₂-CH₄-N₂ ternary mixtures were composed by ~90, 80, 50 and 33.3 mol% CO₂ with equal proportions of N₂ and CH₄, i.e., ~5, 10, 25 and 33.3 mol%, respectively.

2.2 Improved pressurization system

The HPOC system consists of a manual screw pressure-generator, a pump, two pressure-transducers (± 1 bar), and stainless steel microtubes connected by several valves (Chou et al., 2005, 2008; Garcia-Baonza et al., 2012; Caumon et al., 2014). A transparent fused silica micro-capillary (FSC) of 200 μ m internal diameter was sealed at one end by a hydrogen flame (Caumon et al., 2013, 2014) and coupled to the HPOC system by the other end. Then it was set on a customized heating-cooling stage (Linkam CAP500). The temperature of the stage was previously calibrated against the triple point of distilled water (0.0 °C) and of pure CO₂ (-56.6 °C). The system was purged under vacuum for about 30 minutes to remove any other gas before loading the gas mixture into the system. The advantage of our home-made system is that it requires neither mercury nor water for pressurization (Fang et al., 2018; Wang et al., 2019). Indeed, the total effective internal volume of the system is about some dozen μ L (included the volume of the FSC, stainless steel microtubes, and valves), while that of the manual pressure generator is 20 mL. The pressure could be adjusted step-by-step from 5 to 600 bars by turning the manual pressure-generator. Thereby, the gas mixtures were analyzed by Raman spectroscopy through the transparent microcapillary at controlled *PTX* conditions.

2.3 In-situ Raman measurement and data processing

Raman analyses were carried out by a LabRAM HR spectrometer (Horiba Jobin-Yvon®) equipped with an 1800 groove·mm⁻¹ grating and a liquid nitrogen-cooled CCD detector. The apertures of the confocal hole and of the slit width were respectively set at 1000 and 200 μ m giving a spectral resolution of about 1.6 cm⁻¹. The excitation radiation was provided by an Ar⁺ laser (Stabilite 2017, Spectra-Physics) at 514.532 nm with a power of 200 mW, focused in the transparent FSC through a $\times 20$ objective (Olympus, NA = 0.4), or in natural FIs (of sizes <15 μ m) through a $\times 50$ Olympus (Olympus, NA = 0.5). Acquisition time was between 1–30 seconds per accumulation depending on the

nature of the analyzed sample (FCS or natural IFs, the size, shape, and depth of natural FIs) for the optimization of the S/N ratio within a minimum measurement time. Each measurement was repeated successively six times (with ten accumulations per measurement) at the same *PTX* conditions for statistical purposes. A spectrum was recorded before loading any gas mixture into the microcapillary for the subtraction of the signal of atmospheric N₂.

The Raman spectrum of N₂ exhibits a single band corresponding to the stretching vibration mode at ~2331 cm⁻¹, denoted by ν_1 . The variation of the N₂ band as a function of pressure (5-600 bars) and composition (within CO₂-N₂ gas mixtures) was studied in our previous work (Le et al., 2019). This study demonstrated the modest reproducibility of the variation of the position of the N₂ band even after a wavelength calibration by a neon band at 2348.43 cm⁻¹ (cf. Figure 5 in Le et al., 2019). Similar modest reproducibility of N₂ band within CH₄-N₂ mixtures was also observed in the experiments conducted in the present study (see Fig. A.3 in Appendix A). Indeed, although the same tanker containing the CH₄-N₂ mixture was used to repeat the analyses over several days, the obtained position of the N₂ band presented a noticeable difference (leading thus to non-systematic variation as the composition changes), whereas the variation of the peak position of associated CH₄ remained consistent (see section 3.2 below). Moreover, the magnitude of the variation is quite small (<~3 cm⁻¹ at 600 bars) compared to that of CH₄ (~7 cm⁻¹ at 600 bars, see below). Thus, the following sections exclusively report the most reliable spectral parameters, i.e., the variation of the peak position of the ν_1 band of CH₄ (ν_{CH_4}) and the Fermi diad splitting of CO₂ (Δ) as a function of pressure (or density) and composition of gas mixtures.

The Raman spectrum of CH₄ is characterized by a major band corresponding to the symmetric stretching mode (ν_1) at ~2917 cm⁻¹. The Raman spectrum of CO₂ is characterized by two strong bands (denoted ν^+ at ~1385 cm⁻¹ and ν^- at ~1288 cm⁻¹) arising from the so-called Fermi resonance effect occurring between the symmetric stretching vibration mode (ν_1) and the first overtone of bending vibration mode ($2\nu_2$) (Fermi, 1931). Besides, there are two weak bands at the outer sides of both main bands of CO₂ (at ~1409 cm⁻¹ and 1265 cm⁻¹, assigned to hot bands) and a weak band at 1370 cm⁻¹ assigned to the signal ¹³CO₂. Extended interpretation of the spectral features of CO₂ can be found in literature (Placzek, 1934; Amat and Pimbert, 1965; Howard-Lock and Stoicheff, 1971; Bertrán, 1983). Since the intensities of the hot bands are too small, there are not of clear interest for our quantitative calibration purpose. In the present work, the interesting spectral parameters include the ν_1 band of CH₄, and the two main bands ν^+ and ν^- of CO₂.

The spectra of CO₂, N₂ and CH₄ were recorded over three different spectral windows from 1100 to 1580 cm⁻¹, from 2100 to 2525 cm⁻¹ and from 2675 to 3050 cm⁻¹, respectively. They were processed, after baseline subtraction, by an asymmetrical Gaussian-Lorentzian function from the peak fitting tool of LabSpec 6 software (HORIBA). The fitted peak position of the CH₄ band (ν_{CH_4}) was then corrected

($v_{\text{CH}_4}^{\text{corrected}}$) against two closely well-known emission lines of neon (v_{Ne}^1 at 2851.38 cm^{-1} and v_{Ne}^2 at 2972.44 cm^{-1}) using equation 1 of Lin et al. (2007). The reference value of v_{Ne}^1 and v_{Ne}^2 are cited from NIST Chemistry webbook (Kramida et al., 2018). Because the two main bands of CO_2 were recorded by a single measurement and that only the variation of CO_2 Fermi diad splitting (the difference between the two bands) was studied, no peak position correction was required for the case of CO_2 (Fall et al., 2011). The uncertainties of spectral features were determined from six consecutive measurements, yielding an uncertainty of about $\pm 0.4\%$ in peak area values, $\pm 0.01 \text{ cm}^{-1}$ in the fitted peak position of a single band of CH_4 and CO_2 , and $\pm 0.015 \text{ cm}^{-1}$ in Fermi diad splitting value of CO_2 (1σ).

2.4 Microthermometry analyses of natural fluid inclusions

Microthermometry measurements of natural fluid inclusions were performed using a THMS600 heating-cooling stage coupled with an Olympus BX50 microscope. The calibration of temperature was carried out with standard inclusions of pure CO_2 ($-56.6 \text{ }^\circ\text{C}$) and pure H_2O ($0.0 \text{ }^\circ\text{C}$), yielding an uncertainty of about $\pm 0.1 \text{ }^\circ\text{C}$. Natural prismatic quartz crystals (Ta15, Mu618 and Mu1381) were collected in the CH_4 -zone in the late Alpine tension gashes from the Central Alps, Switzerland (Mullis et al., 1994; Tarantola et al., 2007). They contain one- and two-phase $< 25 \text{ }\mu\text{m}$ pseudo-secondary CH_4 -dominated FIs mixed with CO_2 or N_2 . Two-phase aqueous-dominated fluid inclusions hosted in a quartz sample from the W-Cu-Sn deposit of Panasqueira (Portugal) (denoted PAN-V3) were also selected for the analysis of their vapour, which contains a ternary CO_2 – CH_4 – N_2 mixture (Fig. 1) (Noronha et al., 1992; Cathelineau et al., 2017; Carocci et al., 2019; Caumon et al., 2019).

Both homogenization ($T_{\text{h}}(\text{vol})$) and melting ($T_{\text{m}}(\text{vol})$) temperatures of the volatile phase could be observed in the FIs of sample Ta15. Therefore the VX properties could be directly obtained from the VX diagrams for CH_4 – CO_2 gas mixtures of Thiéry et al. (1994). In reason of the very low triple points of CH_4 and N_2 (-182 and $-210 \text{ }^\circ\text{C}$, respectively), measuring the melting temperature of the CH_4 – N_2 mixture in the volatile phase of the FIs of sample Mu1381 was not possible with our heating-cooling stage instrument, which operates in the range -180 to $600 \text{ }^\circ\text{C}$. Also, the melting temperature of CO_2 – CH_4 phases within the FIs of selected Mu618 samples could not be observed due to the small size and the low density of the fluids. Therefore, only the homogenization temperature could be accurately determined, and so the composition of these FIs could only be fully determined from Raman analyses. The molar volume (density) and pressure were obtained from the homogenization temperature and composition of the volatile phases using an appropriate EoS. In the case of the fluid inclusions hosted in sample PAN-V3, no phase transitions were observed in the carbonic phase. Only the existence of clathrate pointed out the presence of low-density gas in these FIs.

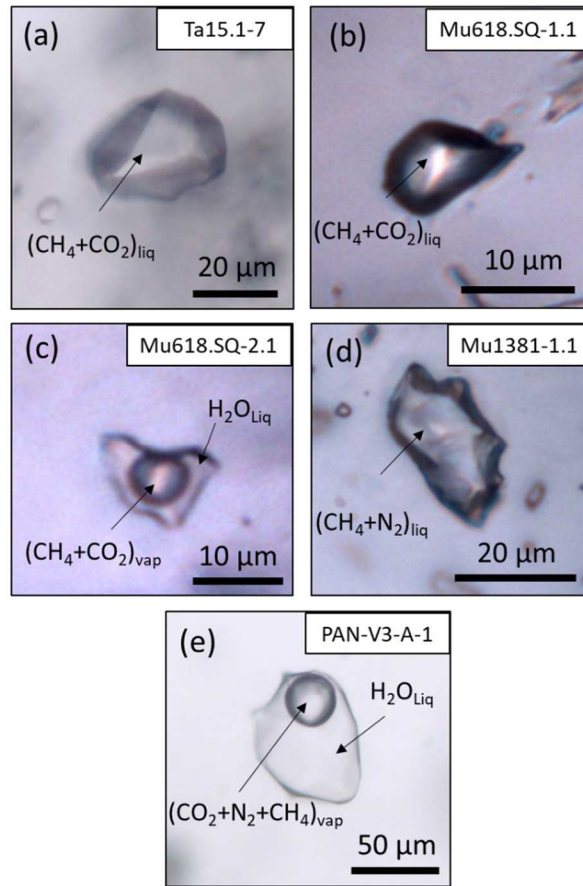


Fig. 1. Microphotographs of selected FIs at room temperature trapped within the sample Ta15.1, Mu168.SQ, Mu1381 and PAN-V3. Monophasic FIs containing a liquid composed of CH₄–CO₂ (a, b) or of CH₄–N₂ (d); Biphasic FI containing H₂O liquid and a bubble of CO₂–CH₄ vapor (c) and of CO₂–N₂–CH₄ vapor (e).

In the present work, the GERG-2004 EoS, integrated into REFPROP software (Lemmon et al., 2013), was chosen because it is known as the most accurate available EoS. Concerning the binary and ternary mixtures of CH₄, CO₂, and N₂, the GERG-2004 EoS were fitted from more than 3300 experimental data points, and cover large pressure and temperature ranges, up to 5000 bars and over –53 to 400 °C (Kunz, 2007). The uncertainties in density were claimed less than 0.5%.

3. Experimental results

3.1 Reevaluation of the RRSCS of CH₄ for molar fraction determination

Based on the polarizability theory of Raman scattering by Placzek (1934), the RRSCS of the ν_1 band of CH₄ (σ_{CH_4}) is calculated from the peak area of CH₄ and N₂ bands (A_{CH_4} and A_{N_2}), their molar fraction (C_{CH_4} and C_{N_2}) and instrumental efficiency at their respective position (ξ_{CH_4} and ξ_{N_2}) using Equation (1) (Pasteris et al., 1988). Since our Raman spectrometer was calibrated using a white lamp of known emission (Raman Calibration Accessory, Kaiser Optical System, Inc) and all Raman spectra were corrected by an ICS function (Intensity Correction System) integrated into Labspec 6 software (HORIBA), the instrumental efficiencies at the wavelength of CH₄ (ξ_{CH_4}) and N₂ (ξ_{N_2}) bands are thereby identical (Dubessy et al., 2012).

$$\sigma_{\text{CH}_4} = \frac{A_{\text{CH}_4} \cdot C_{\text{N}_2} \cdot \xi_{\text{N}_2}}{C_{\text{CH}_4} \cdot A_{\text{N}_2} \cdot \xi_{\text{CH}_4}} \quad (1)$$

σ_{CH_4} was plotted as a function of pressure and composition of CH_4 - N_2 mixtures (Fig. 2). In general, σ_{CH_4} remains constant as pressure increases. The latter result agrees well with the study of Fabre and Oksengorn (1992) where the authors reported the constancy of the peak area ratio up to 3000 bars. A shift between the curves of different concentrations is not significant as this can be due to small errors in the measured composition of gas mixtures. Otherwise, the irregular deviation of the σ_{CH_4} values were observed exclusively at a low-pressure range ($< \sim 70$ bars). A similar deviation of the variation of $A_{\text{CH}_4}/A_{\text{N}_2}$ ratio at low pressure was also observed by Fabre and Oksengorn (1992) and Seitz et al. (1993). This deviation could be explained by two reasons:

- (1) The error in the fitted N_2 peak area and the subtraction of the atmospheric N_2 peak area.

Indeed, the peak of N_2 is asymmetric at low density and becomes more and more symmetric with increasing density (Musso et al., 2002, 2004). Measuring the peak area of an asymmetric band may cause a higher error than for symmetric one. Especially at low pressure, the peak of N_2 in microcapillary (> 5 bars) and in the atmosphere (1 bar) are quite interfered. Besides, the intensity (or area) of the N_2 band at low pressure (or density) is much smaller than that of CH_4 . Thus, a small fluctuation of N_2 intensity (or area) value can result in an important variation of the $A_{\text{CH}_4}/A_{\text{N}_2}$ ratio.

- (2) The variation of the peak area ratio also reflects the change of the effective scattering efficiency of each individual gas that are sensitive to the change of internal field (which is quantified by the refraction index) with increasing density (Eckhardt and Wagner, 1966; Schrötter and Klöckner, 1979; Dubessy et al., 1989). Otherwise, the effect of intermolecular interaction change is rather small at low pressure range, and so negligible (see in the subsection 3.2). According to the experimental data of Fabre and Oksengorn (1992) and Seitz et al. (1993), the internal field increases with density and might reach its maximum at around 50–75 bars, then do not change up to 3 kbar.

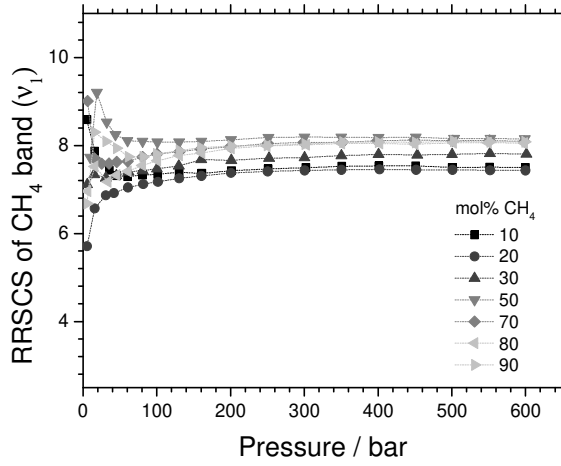


Fig. 2. Pressure and composition dependence of the RRSCS of the CH₄ band (ν_1) in CH₄-N₂ binary mixtures.

Overall, we can now confirm the independence of σ_{CH_4} on pressure (or density) and composition. The average value of the σ_{CH_4} measured from 127 experimental data points over all the studied pressure range is 7.73 ± 0.16 (1σ) corresponding to an error of about ± 0.5 mol%. In the low-pressure range, the uncertainty of the average values of σ_{CH_4} is slightly higher (± 0.3), that in turn, can cause an error of up to ± 2 mol%. However, the latter error can be negligible upon the determination of pressure or density of gas mixture because the effect of the composition on density is not appreciable at < 50 bars (see the following sections). Table 1 shows a comparison of our results to values published in literature. There is a slight difference, but our experiments provide better accuracy. Note that RRSCS of CH₄ was evaluated using an excitation wavelength of 514.5 nm. RRSCS value for other excitation wavelengths can be calculated from result obtained herein using Equation 11 in Garcia-Baonza et al. (2012).

Table 1: Comparison of RRSCSs of CH₄ band (ν_1) at 514.5 nm.

| | This study | Fouche and Chang (1971) | Penney et al. (1972) | Dubessy et al. (1989) | Seitz et al. (1993) |
|------------------------|-----------------|----------------------------|-------------------------|--------------------------|------------------------|
| Pressure (bar) | 5-600 | 2.35 | - | ≤ 1 | 7-700 |
| σ_{CH_4} | 7.73 ± 0.16 | 8.0 | 7.7 ± 0.4 | 7.57 | 7.39 ± 0.2 |

3.2 Evolution of Raman spectral features as a function of composition, pressure, and density

3.2.1 Variation of the CH₄ peak position

Fig. 3a and b represent the variation of the corrected peak position of methane ($\nu_{\text{CH}_4}^{\text{corrected}}$) as a function of pressure and composition in CH₄-N₂ and CO₂-CH₄ gas mixtures, respectively. In general, $\nu_{\text{CH}_4}^{\text{corrected}}$ decreases as pressure increases in both cases. However, the effect of the composition on the variation of $\nu_{\text{CH}_4}^{\text{corrected}}$ is completely different. More discernible composition effects were observed for CH₄-N₂ mixtures than for CO₂-CH₄ ones. Indeed, while pressure increases from 5 to 600 bars the downshift of $\nu_{\text{CH}_4}^{\text{corrected}}$ reduced from $\sim 6.76 \text{ cm}^{-1}$ (pure CH₄) to $\sim 1.86 \text{ cm}^{-1}$ for the CH₄-N₂ mixture of

10 mol% CH₄, but reduced only to 5.90 cm⁻¹ for the CO₂–CH₄ mixture of 10 mol% CH₄. Otherwise, with the diminution of the CH₄ content, the downshift of $v_{CH_4}^{corrected}$ within CH₄–N₂ mixtures gradually decreases over the entire studied pressure range (Fig. 3a), whereas the downshift of $v_{CH_4}^{corrected}$ within CH₄–CO₂ mixtures increases between 80 and ~300–400 bars then decreases as pressure increases further (Fig. 3b). The difference between these variation trends of CH₄ peak position in mixtures with N₂ and CO₂ is further interpreted based on intermolecular interaction changes in the discussion section.

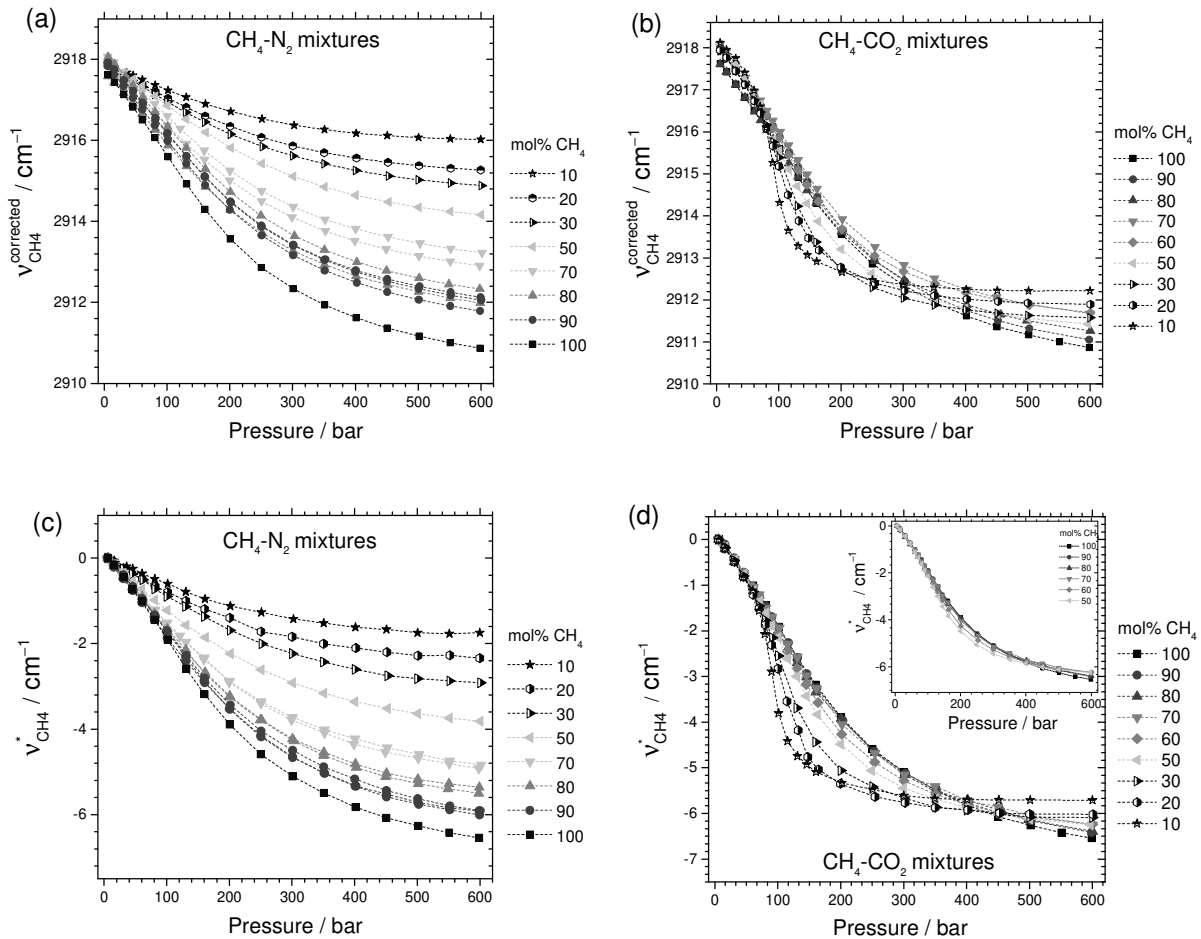


Fig. 3. (a) Variation of the corrected peak position of the v_1 band of CH₄ ($v_{CH_4}^{corrected}$) within CH₄–N₂ gas mixtures as a function of pressure and composition. Reproducibility tests were performed by analyzing two times the mixtures of 70 and 80 mol% CH₄ and three times the mixtures of 90 mol% CH₄. Calibration curves of the same concentration obtained in different days are parallel indicating a day-to-day-systematic error (see text). (b) Variation of $v_{CH_4}^{corrected}$ within CH₄–CO₂ gas mixtures as a function of pressure and composition. (c) Relative variation of the fitted CH₄ peak position ($v_{CH_4}^*$) as a function of pressure and composition of CH₄–N₂ and (d) CH₄–CO₂ gas mixtures. The insert in figure (d) is plotted only for calibration data for the mixtures of ≥ 50 mol% CH₄.

Reproducibility tests were performed by analyzing two or three times the mixtures of 70, 80 and 90 mol% CH₄. The calibration curves of the same concentrations (represented in Fig. 3a) obtained at different days are parallel, indicating a systematic day-to-day error. The latter error can be explained by the fact that our neon lamp was not permanently fixed in the optical path of the Raman spectrometer, resulting in the variation of the shape and so, of the fitted peak position of the neon

lines. That, in turn, leads to a variation upon the peak position correction using Equation (1) in Lin et al. (2007). As a result, the whole data set collected within the same day was shifted by an identical error. This problem was also reported in our previous study of the N₂ peak position within the CO₂–N₂ mixtures (Le et al., 2019). Therefore, a higher-accurate method of wavelength correction is needed for any quantitative measurements based on the absolute corrected peak position value. To avoid the day-to-day systematic error, we studied the relative variation (or the variation of the downshift) of the fitted CH₄ peak position ($v_{\text{CH}_4}^*$) calculated by Equation (2), where $v_{\text{CH}_4}^i$ is the fitted peak position of CH₄ measured at i bar (i ranges from 5 to 600 bars), $v_{\text{CH}_4}^{5 \text{ bar}}$ is the fitted peak position of CH₄ at ~5 bars of a standard (cf. Appendix A).

$$v_{\text{CH}_4}^* = v_{\text{CH}_4}^i - v_{\text{CH}_4}^{5 \text{ bar}} \quad (2)$$

Fig. 3c represents the variation of $v_{\text{CH}_4}^*$ as a function of pressure and composition of CH₄–N₂ gas mixtures. The curves of 70 and 90 mol% CH₄ are now nearly superimposed and can be clearly distinguished from the curve of 80 mol% CH₄, indicating the excellent reproducibility of $v_{\text{CH}_4}^*$ all over the studied pressure-composition range (Fig. 3c). The reproducibility of $v_{\text{CH}_4}^*$ was also improved for the case of CH₄–CO₂ mixtures (Fig. 3d). Compared with Fig. 3b, the evolution of the calibration curves represented in Fig. 3d shows a better correlation with the variation of mixture compositions.

The total pressure of the gas mixtures of known composition at a given temperature was converted to density using GERG-2004 EoS. Fig. 4a and b represent the relationships between $v_{\text{CH}_4}^*$, the calculated density and the composition of CH₄–N₂ and CO₂–CH₄ gas mixtures, respectively, which can be used as densimeters for direct density determination.

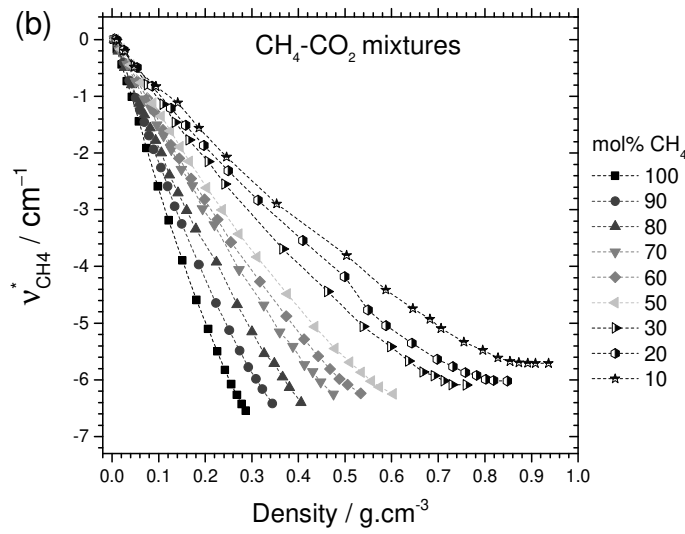
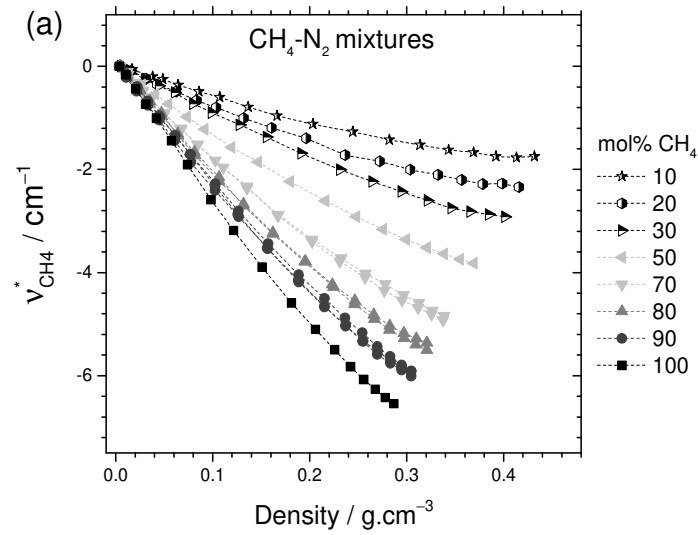


Fig. 4. Relative variation of the fitted CH_4 peak position ($v_{\text{CH}_4}^*$) as a function of density and composition of (a) $\text{CH}_4\text{-N}_2$ and (b) $\text{CH}_4\text{-CO}_2$ gas mixtures. The density was calculated from a given pressure and composition using GERG-2004 EoS.

3.2.2 Variation of the CO_2 Fermi diad splitting

The relationship between the Fermi diad splitting of CO_2 (Δ), pressure, and composition of the $\text{CO}_2\text{-CH}_4$ gas mixture plotted in Fig. 5 shows similar behavior with that observed for $\text{CO}_2\text{-N}_2$ gas mixtures (cf. Fig. 6 in Le et al. (2019)). In general, Δ increases with increasing pressure. The effect of composition on the variation of Δ is rather small at low-pressure but more pronounced at high-pressure. For instance, the magnitude of the total Δ variation of pure CO_2 is about $\sim 2.583 \text{ cm}^{-1}$ (increased from 102.765 cm^{-1} at 5 bars to 105.348 cm^{-1} at 600 bars) and gradually diminishes with the increase of the CH_4 content, down to $\sim 0.5 \text{ cm}^{-1}$ for the $\text{CO}_2\text{-CH}_4$ of 90 mol% CH_4 (Fig. 5).

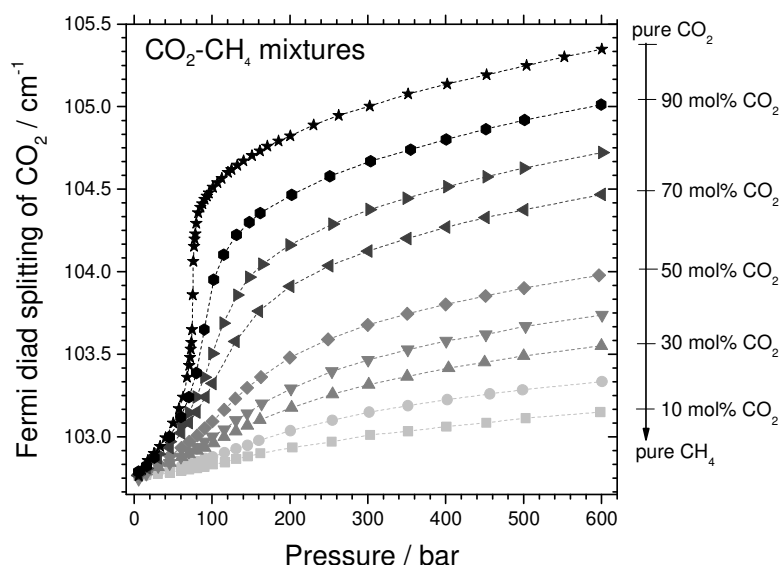


Fig. 5. Variation of CO₂ Fermi diad splitting (Δ) at 32 °C as a function of pressure and composition of CO₂–CH₄ gas mixtures.

The variation of Δ as a function of density (calculated from a given pressure, temperature and composition using GERG-2004 EoS) and composition of the CO₂–CH₄ gas mixture is plotted in Fig. 6. Δ increases with increasing CO₂ content and density of the gas mixture. Otherwise, a drastic increase of Δ value was observed for the pure CO₂ at ~74 bars (Fig. 5). It is because all Raman analyses were made at ~32 °C, very close to the critical point of CO₂. At that *PT* point, a small fluctuation of either pressure or temperature can result in a significant variation of density. Besides, we noted that the Δ -density calibration curve of pure CO₂ is nearly superimposed with that of the mixture with 10 mol% CH₄ which agrees well with the statement of Wang et al. (2011) “*The calibration data of pure CO₂ can be applied for CO₂–CH₄ mixtures of less than 10 mol% CH₄*”. For instance, at $\Delta = 105 \text{ cm}^{-1}$, the calculated pressure for pure CO₂ and for the CO₂–CH₄ mixture of 10 mol% CH₄ is 293 and 561 bars, respectively (268 bars of difference), but the calculated densities are very close, i.e., 0.940 g·cm⁻³ for pure CO₂ and 0.925 g·cm⁻³ for the mixture (0.015 g·cm⁻³ of difference).

Overall, the experimental results indicate that Δ is a reliable parameter for monitoring pressure (or density) of CO₂–CH₄ mixtures. Notably, it presents a good reproducibility without any wavelength correction, making it a robust and practical spectral parameter for quantitative analysis.

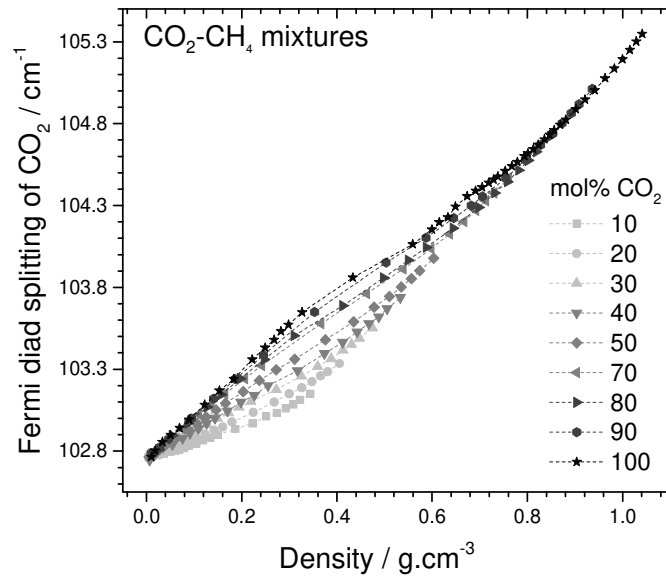


Fig. 6. Variation of CO₂ Fermi diad splitting (Δ) as a function of density and composition of CO₂–CH₄ gas mixtures. The density was calculated by GERG-2004 EoS at a given temperature, pressure, and composition.

3.2.3 Effect of temperature on the variation of Raman spectral parameters

All calibration data presented above were performed at 32 °C (above the critical temperature of pure CO₂) to avoid the biphasic L-V domain of any gas mixtures, and to combine with the calibration data set of Le et al. (2019) for ternary mixtures analyses. The calibration of CO₂–CH₄ mixtures was also performed at 22 °C to examine the effect of temperature on the variation of Δ and $\nu_{\text{CH}_4}^*$ with pressure (or density) and composition. All calibration data obtained at 22 °C can be found in Appendix B (Fig. B.1 and B.3) and in Supplementary Material.

The effect of temperature on the variation of Δ for CO₂–CH₄ mixtures is very similar to that observed for CO₂–N₂ mixtures (Le et al., 2019) (Fig. B.2 in Appendix B). Indeed, at the same pressure and composition, Δ is shifted toward higher wavenumbers at 22 °C compared to 32 °C (Fig. B.2-a). However, the Δ -density relationships obtained at 22 et 32 °C are almost superimposed (Fig. B.2-b). Slight differences, of up to 0.02 g·cm⁻³, are noticed for some concentration ranges in good agreement with the observation of Wang et al. (2011) and Wang et al. (2019).

Also, the effect of temperature was observed for the variation of $\nu_{\text{CH}_4}^*$ as a function of pressure and composition with a downshift toward lower wavenumbers as temperature decreases (Fig. 7a). Fig. 7b presents the variation of $\nu_{\text{CH}_4}^*$ as a function of density, composition, and temperature. Overall, the difference between the two calibration data sets obtained at 22 and 32 °C is discernible but rather small, less than about 0.015 g·cm⁻³. The latter observations confirm that the calibration should be dedicatedly provided for each temperature to minimize the error due to the effect of temperature on the variation of spectral parameters.

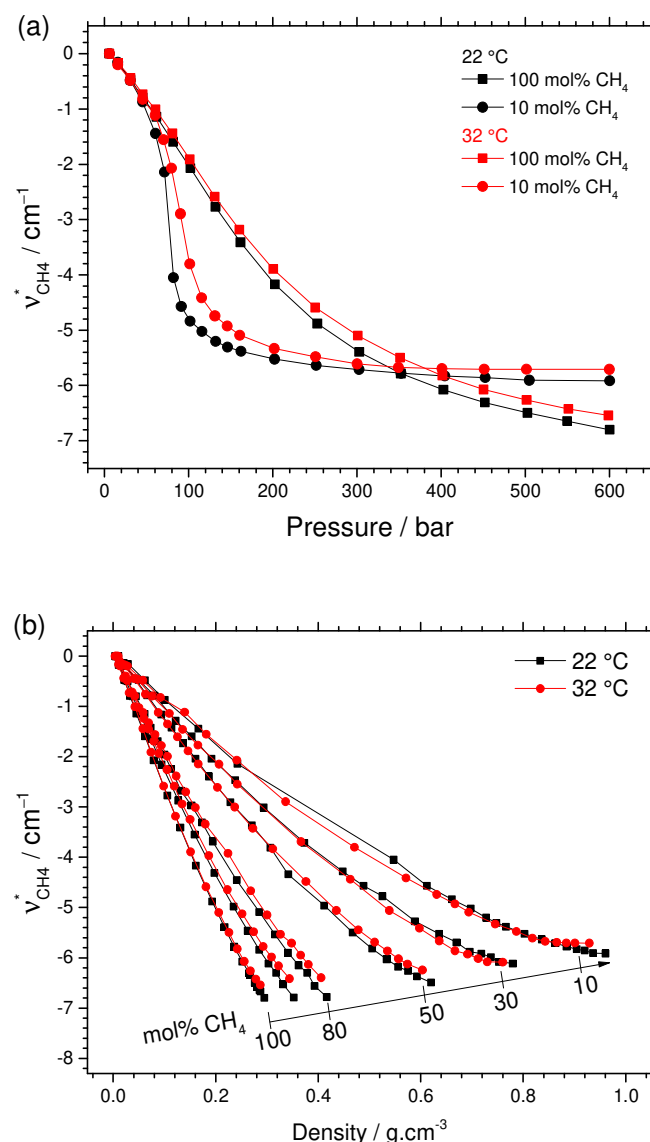


Fig. 7. Effect of temperature on the variation of $v_{CH_4}^*$ as a function of (a) pressure and (b) density of CO_2-CH_4 mixtures.

3.3 Calibration polynomial equations for pressure and density determination

3.3.1 Determination of pressure and density of CH_4-N_2 and CO_2-CH_4 binary gas mixtures

Both Δ and $v_{CH_4}^*$ can be used as a parameter sensitive to the variation of pressure (or density) and composition for the determination of pressure and density of gas mixtures. Note that Δ can be directly measured from any CO_2 Raman spectrum whereas $v_{CH_4}^*$ requires a reference value of the peak position of pure CH_4 (or mixtures of CH_4) at 5 bars ($v_{CH_4}^{5\text{ bar}}$) according to Equation (2). A sealed transparent microcapillary containing ~ 5 bars (± 1) of pure CH_4 were made for the wavelength correction (called CH_4 standard, Fig. A.2 – Appendix A). The CH_4 standard should be analyzed before and/or after analyzing the actual sample to evaluate any spectrometer calibration deviation.

In the CH_4-N_2 gas mixtures, only $v_{CH_4}^*$ could be used for pressure and density measurement. The variation of the N_2 peak position should not be used because of its moderate reproducibility (see Fig.

A.3 – Appendix A, and Figure 5 in Le et al. (2019)). The experimental data plotted in Fig. 3c, and Fig. 4a were fitted by the polynomial Equation (3), linking pressure (P) or density (ρ) to CH_4 concentration (C_{CH_4}) and $v_{\text{CH}_4}^*$, where a_{ij} (with $i + j \leq 4$) are the coefficients of the best-fitting regression models. To decrease the uncertainty on the measurement of pressure and density, experimental data were independently fitted for two different composition domains (\geq and ≤ 50 mol% CH_4). The coefficients a_{ij} fitted for each domain are listed in Table 2. The uncertainties reported in the last row of Table 2 were derived from the prediction bounds of the fitting model at 1σ .

$$P \text{ (or } \rho) = \sum_{i=0}^3 \sum_{j=0}^4 a_{ij} \cdot (C_{\text{CH}_4})^i \cdot (v_{\text{CH}_4}^*)^j \quad (3)$$

Table 2: Fitted coefficients (a_{ij}) of Equation (3) for the determination of pressure (P) and density (ρ) of CH_4 – N_2 gas mixtures. Calibration equations were given for two mixture composition domains (\geq and ≤ 50 mol% CH_4). The uncertainties on calculated pressure and density were derived from the prediction intervals of the regression polynomial at 1σ

| Coefficients | Pressure determination (bar) | | Density determination ($\text{g}\cdot\text{cm}^{-3}$) | |
|---------------------------|---------------------------------|---------------------------------|---|---------------------------------|
| | ≥ 50 mol% CH_4 | ≤ 50 mol% CH_4 | ≥ 50 mol% CH_4 | ≤ 50 mol% CH_4 |
| a_{00} | -172.82 | -37.14 | -0.06753 | 0.01993 |
| a_{10} | 862.35 | 746.68 | 0.3112 | -0.08883 |
| a_{01} | -188.59 | -197.31 | -0.2024 | -0.1465 |
| a_{20} | -1346.66 | -3310.32 | -0.4362 | 0.02792 |
| a_{11} | 644.02 | 1388.21 | 0.5052 | 0.1963 |
| a_{02} | 68.58 | 97.16 | 0.02588 | 0.06475 |
| a_{30} | 678.52 | 4097.22 | 0.1984 | 0.2052 |
| a_{21} | -1217.18 | -6921.35 | -0.5917 | -0.7082 |
| a_{12} | -272.09 | -1024.40 | -0.06615 | -0.5293 |
| a_{03} | -16.01 | -48.88 | -0.00212 | -0.01924 |
| a_{31} | 767.45 | 10121.08 | 0.2576 | 1.559 |
| a_{22} | 248.60 | 2221.96 | 0.04373 | 0.9825 |
| a_{13} | 29.09 | 223.16 | 0.00294 | 0.07004 |
| a_{04} | 1.279 | 10.04 | 8.673e-05 | 0.002134 |
| Adjusted R^2 | 0.9976 | 0.9946 | 0.9995 | 0.9988 |
| Uncertainty (1σ) | ± 11 | ± 18 | ± 0.003 | ± 0.006 |

Regarding the CO_2 – CH_4 mixtures, since the $v_{\text{CH}_4}^*$ of the mixtures of <50 mol% CH_4 becomes less sensitive to the variation of pressure above ~ 200 bars, in the following we consider only calibration data of the mixtures dominated by CH_4 (≥ 50 mol% CH_4) for regression analysis (insert of Fig. 3d and

Fig. 4b). Experimental data of $v_{\text{CH}_4}^*$ in CH_4 -dominated mixtures were therefore fitted by polynomial Equation (4). Every coefficient b_{ij} (with $i + j \leq 4$) and uncertainty of the best-fitting equations were listed in Table 3.

$$P \text{ (or } \rho) = \sum_{i=0}^3 \sum_{j=0}^4 b_{ij} \cdot (C_{\text{CH}_4})^i \cdot (v_{\text{CH}_4}^*)^j \quad (4)$$

Table 3: Fitted coefficients (b_{ij}) of Equation (4) for determination of pressure (P) and density (ρ) of CO_2 – CH_4 gas mixtures. Calibration equations were only given for the mixtures of ≥ 50 mol% CH_4 . The uncertainties on the calculated pressure were derived from the prediction interval of the regression polynomial at 1σ

| | For pressure determination (bar) | For density determination ($\text{g}\cdot\text{cm}^{-3}$) |
|---------------------------|--|---|
| X domains Coefficients | ≥ 50 mol% CH_4 | ≥ 50 mol% CH_4 |
| b_{00} | 16.99349 | - 0.003751 |
| b_{10} | -75.74656 | 0.07936 |
| b_{01} | -35.59074 | -0.060703 |
| b_{20} | 139.47675 | -0.155453 |
| b_{11} | -150.71132 | -0.106032 |
| b_{02} | -20.60863 | 0.003617 |
| b_{30} | -63.05569 | 0.08733 |
| b_{21} | 359.92530 | 0.217043 |
| b_{12} | 83.88300 | -0.005841 |
| b_{03} | 6.20787 | -0.000248 |
| b_{31} | -175.56035 | 0.07916 |
| b_{22} | -20.17127 | 0.006827 |
| b_{13} | 6.95781 | 0.001283 |
| b_{04} | 1.31372 | 0.0001002 |
| Adjusted R^2 | 0.9963 | 0.9996 |
| Uncertainty (1σ) | ± 15 | ± 0.004 |

Pressure and density of CO_2 – CH_4 gas mixtures can also be determined from Δ , especially for the CO_2 -dominated mixtures (<50 mol% CH_4). The experimental data of Δ reported in Fig. 5 and Fig. 6 were fitted by a fourth-order polynomial. The general formula of the best-fitting regression model is expressed by Equation (5), where \bar{C}_{CO_2} and $\bar{\Delta}$ are respectively defined by Equation (1), (6), and (7), C_{CO_2} is the concentration of CO_2 in CO_2 – CH_4 gas mixtures, c_{ij} (with $i + j \leq 4$), h , k Std_h and Std_k are coefficients of the best-fitting regression models. In order to minimize the uncertainty on pressure

and density from best-fitting models, the calibration data were divided into four smaller pressure-composition (*PX*) domains. The obtained coefficients and uncertainties of the best-fitting equations of every *PX* domains were listed in Table 4 for pressure determination (bar) and Table 5 for density determination ($\text{g}\cdot\text{cm}^{-3}$).

$$P \text{ (or } \rho) = \sum_{i=0}^3 \sum_{j=0}^4 c_{ij} \cdot (\bar{C}_{\text{CO}_2})^i \cdot \bar{\Delta}^j \quad (5)$$

where:

$$\bar{C}_{\text{CO}_2} = \frac{C_{\text{CO}_2} - h}{\text{Std}_h} \quad (6)$$

$$\bar{\Delta} = \frac{\Delta - k}{\text{Std}_k} \quad (7)$$

Table 4: Fitted coefficients of Equation (5) for the determination of pressure of CO_2 – CH_4 gas mixtures. Experimental data were fitted over four different *PX* domains in order to minimize uncertainty. The uncertainties on the calculated pressure of each best-fitting equation were derived from the prediction intervals of the regression polynomial at 1σ .

| <i>PX</i> domains Coefficients | 50-100 mol% CO_2 | | 10-50 mol% CO_2 | |
|-----------------------------------|---------------------------|-----------|--------------------------|-----------|
| | 5-600 bar | 5-160 bar | 5-600 bar | 5-160 bar |
| c_{00} | 117.48157 | 94.656228 | 160.30964 | 86.45553 |
| c_{10} | -64.00435 | -29.90432 | -70.7304 | -36.98006 |
| c_{01} | 75.902022 | 31.9463 | 143.1939 | 63.38251 |
| c_{20} | 33.79624 | 11.05019 | 61.43567 | 16.24622 |
| c_{11} | -153.2075 | -41.39264 | -118.0653 | -18.99735 |
| c_{02} | 110.19830 | -5.575568 | 44.22433 | -9.01309 |
| c_{30} | -17.72552 | -2.412150 | -30.10597 | -3.58623 |
| c_{21} | 81.79481 | 21.269723 | 94.64936 | 5.9654 |
| c_{12} | -148.3062 | -39.40095 | -88.33662 | 11.75184 |
| c_{03} | 93.93866 | 33.513762 | 40.28167 | 0.85861 |
| c_{31} | -13.57701 | -1.313218 | -35.52924 | -2.43154 |
| c_{22} | 43.93126 | 10.23037 | 39.00078 | -5.96449 |
| c_{13} | -49.64265 | -22.26971 | -20.5409 | -1.512 |
| c_{04} | 10.75316 | 7.070998 | 0.75141 | -1.51232 |
| h | 0.82613 | 0.83997 | 0.3022 | 0.3022 |
| Std_h | 0.1781 | 0.17804 | 0.1414 | 0.14182 |
| k | 103.86 | 103.53 | 103.09 | 102.92 |
| Std_k | 0.74857 | 0.63658 | 0.30473 | 0.13981 |
| Adjusted R^2 | 0.9982 | 0.9980 | 0.9987 | 0.9885 |
| Uncertainty (1σ) | ± 10 | ± 3 | ± 8 | ± 6 |

498 Table 5: Fitted coefficients of Equation (5) for the determination of density of CO₂–CH₄ gas mixtures.
 499 Experimental data were fitted over four different *PX* domains in order to minimize the uncertainty of
 500 measurements. The uncertainties on the calculated pressure of each best-fitting equation were derived from the
 501 prediction intervals of the regression polynomial at 1 σ .

| <i>PX</i> domains Coefficients | 50-100 mol% CO ₂ | | 10-50 mol% CO ₂ | |
|-----------------------------------|-----------------------------|------------|----------------------------|-----------|
| | 5-600 bar | 5-160 bar | 5-600 bar | 5-160 bar |
| c ₀₀ | 0.486313 | 0.318294 | 0.22219 | 0.10363 |
| c ₁₀ | -0.041249 | -0.03372 | -0.05087 | -0.02684 |
| c ₀₁ | 0.369020 | 0.295141 | 0.20111 | 0.09192 |
| c ₂₀ | -0.001314 | 0.003835 | 0.009753 | 0.01111 |
| c ₁₁ | -0.003488 | -0.03453 | -0.02361 | -0.01222 |
| c ₀₂ | -0.00996 | 0.03615 | -0.008584 | -0.002226 |
| c ₃₀ | -0.0002312 | -0.001593 | -0.0004959 | -0.002867 |
| c ₂₁ | -0.0135392 | 0.004029 | -0.008539 | 0.001242 |
| c ₁₂ | 0.037468 | 0.006008 | 0.02996 | 0.01194 |
| c ₀₃ | -0.030967 | -0.005571 | -0.009055 | -0.003394 |
| c ₃₁ | 0.001645 | 0.0004832 | 0.00217 | -0.002554 |
| c ₂₂ | -0.0102471 | -0.0008909 | -0.01292 | -0.006362 |
| c ₁₃ | 0.0124289 | 0.008034 | 0.005291 | 0.0005239 |
| c ₀₄ | -0.002157 | -0.008589 | -0.0007252 | 0.0007116 |
| h | 0.82613 | 0.83997 | 0.3022 | 0.3022 |
| Std_h | 0.1781 | 0.17804 | 0.1414 | 0.14182 |
| k | 103.86 | 103.53 | 103.09 | 102.92 |
| Std_k | 0.74857 | 0.63658 | 0.30473 | 0.13981 |
| Adjusted R ² | 0.9997 | 0.9994 | 0.9992 | 0.9940 |
| Uncertainty (1 σ) | ± 0.008 | ± 0.008 | ± 0.006 | ± 0.006 |

502

503 3.3.2 Determination of pressure and density of CO₂–CH₄–N₂ ternary mixtures

504 Fig. 8 shows a comparison between the variation of Δ as a function of pressure and composition of
 505 CO₂ within CO₂–CH₄, CO₂–N₂ and CO₂–CH₄–N₂ mixtures. The experimental data of CO₂–CH₄ and
 506 CO₂–CH₄–N₂ mixtures are from this study, whereas that of CO₂–N₂ mixtures are from the study of Le
 507 et al. (2019). Overall, the variations of Δ within binary and ternary mixtures as a function of pressure
 508 and composition are very similar, indicating that Δ could be used as a quantitative parameter not only
 509 to determine pressure and density of binary (as described in section 3.2.2), but also of CO₂–CH₄–N₂
 510 ternary mixtures. The pressure of CO₂–N₂ mixture (P_2) is systematically higher than that of CO₂–CH₄
 511 mixtures (P_1) at the same value of Δ and molar proportion of CO₂ (insert in Fig. 8). The difference

between the measured pressure P_2 and P_1 can be negligible at low pressure-range (<100 bars) but becomes more appreciable at elevated pressures. The most significant difference between the two calibration data sets was noticed for the curves of 50 mol% CO₂ (up to 150 bars at $\Delta = 102.85 \text{ cm}^{-1}$). Most importantly, for a given CO₂ concentration, the experimental calibration curves of ternary mixtures are always in the middle of the two curves of CO₂–CH₄ and CO₂–N₂ binary mixtures (Fig. 8). For instance, the curve 80-10-10 (XCO₂-XCH₄-XN₂) is in the middle of the 80-20 XCO₂-XCH₄ and XCO₂-XN₂. Note that the molar proportion of CH₄ and N₂ within our ternary mixtures are equal, and the pressure P of the CO₂–CH₄–N₂ ternary mixtures (at a given value of Δ and mol% CO₂) is approximately the mean of (P_1+P_2) (cf. the insert in Fig. 8). According to our analytical analyses (Appendix C), the a/b ratio varies somewhat by a linear function of the molar fraction of CH₄ and N₂ (with a and b the difference between P_1 or P_2 and P , cf. insert in Fig. 8). Thereby, the pressure (P) of ternary mixtures can be deduced from the “nominated” pressures P_1 and P_2 (which are calculated from calibration equations of the binary mixtures described above) using Equation (8), where a and b are now the molar proportions of N₂ and CH₄ in the ternary mixture, respectively.

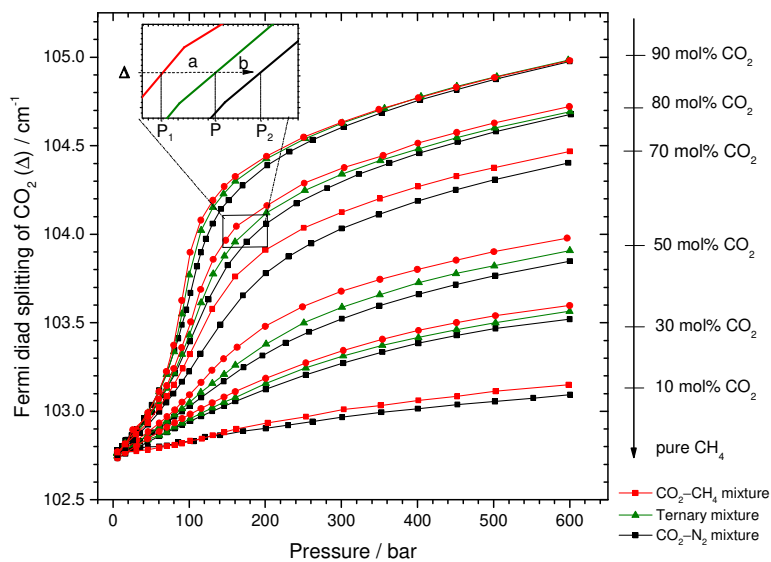


Fig. 8. Variation of CO₂ Fermi diad splitting (Δ) as a function of pressure and composition. The experimental data of CO₂–CH₄ binary mixture, of CO₂–N₂ binary mixture, and of CO₂–CH₄–N₂ ternary mixture are represented by red, black and green points, respectively. The solid lines are a guide for the eye. The concentration of CO₂ within binary and ternary gas mixtures is indicated in the figure. The molar proportion of N₂ and CO₂ within the ternary mixtures is equal. Overall, the calibration curves of the ternary mixtures are always in the middle of the two calibration curves of the binary mixtures at a given CO₂ concentration (see insert).

$$P = \frac{aP_2 + bP_1}{a + b} \quad (8)$$

Once the composition and the pressure of the ternary mixture are determined, the density can be calculated by using an appropriate EoS, or similarly deduced from the corresponding calibration equations dedicated to density determination of binary systems provided above.

3.3.3 Uncertainty analyses

The uncertainty of the final composition, pressure, and density calculated from Raman measurements is contributed by two main sources of error. The first one, denoted $u1$, arises from the best-fitting models obtained by the least-square regression analysis of the experimental data. It reflects how well the calibration equations reproduce the pressure (or density) of the mixture from a given concentration (C_{CH_4} or C_{CO_2}) and Δ or $\nu_{CH_4}^*$. This uncertainty was derived from the prediction intervals (at 1σ) of each best-fit regression equation and reported in the last row in Table 2, Table 3, Table 4, and Table 5.

However, concentration (C_{CH_4} or C_{CO_2}) and spectral features (Δ or $\nu_{CH_4}^*$) were measured with a certain uncertainty. In the present study, the uncertainty of each spectral feature was calculated from six Raman spectra recorded at the same P - T - X conditions (see method section above). Thereby, the uncertainty of a single fitted peak position of CH_4 and CO_2 (ν_{CH_4} , ν^+ , ν^-) is about $\pm 0.01\text{ cm}^{-1}$, and so the uncertainty of $\nu_{CH_4}^*$ and Δ is about $\pm 0.015\text{ cm}^{-1}$ (denoted $i1$). Besides, the uncertainties of the RRSCS of CH_4 (± 0.16 , this study) and of CO_2 (± 0.04 , Le et al., 2019) result in uncertainty of $\sim \pm 0.5\text{ mol\%}$ on the measured composition (denoted $i2$). Thus, the second source of uncertainty (denoted “ $u2$ ”) is the one that relates to the uncertainty $i1$ and $i2$. Since the regression calibration equations are not linear (up to fourth-order polynomial), the uncertainties $i1$ and $i2$ can cause either significant error or less, depending on the mixture composition and pressure (or density) range. Indeed, the uncertainty calculated for a gas mixture of $<50\text{ mol\% } CH_4$ is expected to be higher than that of a mixture of $>50\text{ mol\% } CH_4$ because the sensitivity of $\nu_{CH_4}^*$ to the variation of pressure decreases with the decrease of the CH_4 content (e.g., the curve of $10\text{ mol\% } CH_4$ is much less steep than the curve of pure CH_4) (Fig. 3a). For example, the $\nu_{CH_4}^*$ value = $-1.800 \pm 0.015\text{ cm}^{-1}$ can cause a fluctuation of 22 bars for the CH_4 - N_2 mixture of $10\text{ mol\% } CH_4$ ($\sim 558\text{ bars}$ at $\nu_{CH_4}^* = -1.815\text{ cm}^{-1}$, and $\sim 536\text{ bars}$ at $\nu_{CH_4}^* = -1.785\text{ cm}^{-1}$) but only 2 bars for pure CH_4 . Similarly, the $\Delta = 103.300 \pm 0.015\text{ cm}^{-1}$ causes a fluctuation of 44 bars for the CO_2 - CH_4 mixture of $10\text{ mol\% } CO_2$ but only 2 bars for pure CO_2 . Thus, the uncertainty $u2$ arising from uncertainties $i1$ and $i2$ should be individually estimated for each measurement. More details in the calculation procedure of uncertainty propagation can be found in Supporting Information of Le et al. (2019).

The ultimate uncertainty on the calculated pressure and density can be estimated by the sum of these two error components ($u1$ and $u2$) (Fall et al., 2011; Wang et al., 2011). Overall, the uncertainty of our calibration data is comparable or even better than those of the calibration for pure components published in literature. For example, the calibration data established for pure CO_2 by Wang et al. (2011) yields the uncertainty of $\sim 33\text{ bars}$ and less than about $0.025\text{ g}\cdot\text{cm}^{-3}$ over a pressure range from 22 - 357 bars at room temperature. Regarding the peak position of CH_4 , the pure CH_4 calibration data proposed by Lin et al. (2007) cover a pressure range of up to 600 bars with an uncertainty similar to the one in the present study ($\sim \pm 10\text{ bars}$). Our calibration equations, however, can be applied to any relevant mixture composition.

4. Discussion

4.1 Interpretation of the CH₄ peak position variation with pressure (density) and composition

As the peak position shift is due to the fundamental changes in intermolecular interactions at the molecular scale (Ben-Amotz et al., 1992; Zhang et al., 2016), the difference between the variation trend of the CH₄ peak position in the mixtures with N₂ or CO₂ (Fig. 3) could be partially explained by the change of the intermolecular separation r (Å). According to the Lennard-Jones 6-12 potential approximation, the intermolecular potential consists of a contribution of attractive (dispersion) and repulsive forces which vary as a function of the intermolecular separation r (Jones and Chapman, 1924). At very low pressure (low density), the intermolecular distance r is large enough as such gaseous molecules are completely independent (no interactions between molecules). As pressure increases, the distance between molecules is reduced, and so molecules begin to interact with one another with more frequent collisions and steric restrictions, which impact the vibration mode of gaseous molecules (i.e., lengthening or shortening of C-H bond length of CH₄, perturbing electron cloud distribution, and so resulting to a small change in polarizability, etc.). Firstly, the attractive forces appear and dominate, whereas the repulsive forces are negligible (cf. Fig. D.1 – Appendix D). With further increase of pressure (decrease of the intermolecular distance r), the attractive force increases and reaches its maximum value at a distance r_0 , and the repulsive force also increases and completely compensates the attractive force at $r = \sigma$ (with $r_0 = 1.1224\sigma$). In general, the attractive forces cause a redshift (shifts toward lower wavenumbers) whereas the repulsive ones cause a blueshift (shifts toward to higher wavenumbers) (Zakin and Herschbach, 1986; Lin et al., 2007).

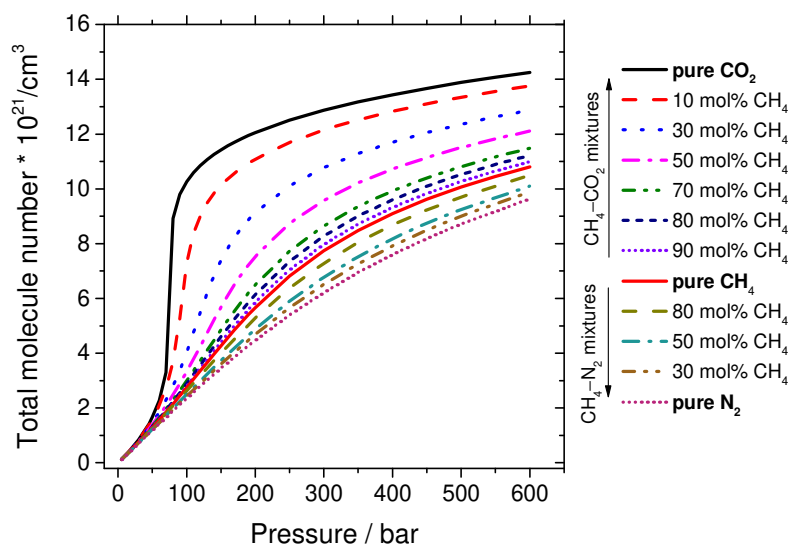


Fig. 9. Evolution of density (molecule number.cm⁻³) of CO₂-CH₄ and CH₄-N₂ mixtures as a function of pressure (bar) and composition at 32 °C.

Regarding CH₄-N₂ mixtures, the total number of gaseous molecules per volume unit steadily increases as pressure increases (Fig. 9), leading to a decrease in the distance r between molecules. However, the

intermolecular distance r is in the range such that the attractive forces between them always dominate and the repulsive forces are insignificant (cf. Fig. D.1 – Appendix D). Over the studied pressure range (5–600 bars), the attractive forces become more and more important with increasing pressure, resulting in the continuous downshift of the CH₄ peak position (Fig. 3c). In addition, the total number of molecules per volume unit also decreases (so, r increases) as the CH₄ proportion decreases (Fig. 9), leading to the decrease of the peak shift magnitude with decreasing CH₄ content (Fig. 3a and c).

On the contrary to CH₄–N₂ mixtures, the total number of molecules per volume unit within CH₄–CO₂ mixtures increases (corresponding to a decrease of r) as the CH₄ content decreases (Fig. 9). The relationship between the CH₄ peak position and pressure is nearly unchanged for the mixtures of ≥ 70 mol% CH₄ (insert of Fig. 3d), indicating that there is no (or little) change in the sum of attractive and repulsive forces, even when the intermolecular distance r slightly decreases. This suggests that intermolecular distance r reaches the vicinity of the r_0 value and the repulsive forces now become more important. Indeed, at that density range ($\sim 11 \cdot 10^{21}$ molecules·cm⁻³), when decreasing the distance between molecules, the repulsive forces become more important and partly compensate the attractive forces. For the CH₄–CO₂ mixtures dominated by CO₂ (<30 mol% CH₄), the total molecule number drastically increases from 70 bars and quickly reaches $\sim 11 \cdot 10^{21}$ molecules·cm⁻³ at around 200–300 bars (Fig. 9), resulting in a noticeable downshift in CH₄ peak position. Then, the density slowly increases as the pressure further increases from 200 to 600 bars, explaining the stepwise behavior of the calibration curve of the CO₂ dominated mixtures. With a further increase of pressure, the repulsive forces would certainly dominate, leading to a peak shift to higher wavenumber, from over ~ 1300 bars as shown by Fabre and Oksengorn (1992) and Zhang et al. (2016) (cf. Fig. D.1 – Appendix D).

4.2 Validation of the calibration data with natural fluid inclusions

The selected natural FIs containing CO₂–CH₄ (samples Ta15 and Mu618), CH₄–N₂ (sample Mu1381), and CO₂–CH₄–N₂ (sample PAN-V3) mixtures were first analyzed by microthermometry in order to observe significative phase transitions for the determination of composition and density. Quartz samples were cooled to temperatures down to -160 °C in order to permit the appearance of a vapor bubble and of a solid phase. The homogenization temperature of the volatile phase $T_h(\text{vol})$, determined by observing the disappearance of the vapor bubble, ranged from -105 to -110 °C for CO₂–CH₄ FIs within sample Ta15, from -74.9 to -89.0 °C for CO₂–CH₄ FIs within sample Mu618 and from -101.2 to -103.7 °C for CH₄–N₂ FIs within sample Mu1381. Melting temperatures of the volatile phase were only accurately determined within FIs of sample Ta15 between -95 and -103 °C. Thereby, the density of FIs of sample Ta15 were directly obtained from the VX diagram of Thiéry et al. (1994), whereas that of FIs of samples Mu618 and Mu1381 could be only calculated using GERG-2004 EoS from the combination of $T_h(\text{vol})$ and the composition obtained from Raman measurement.

Because of the low density of the gas bubble in FI Mu618.SQ-2.1, no phase transition was observed. Also, no phase transition within the volatile part of FIs of sample PAN-V3 could be observed due to

their low density and complex composition (ternary mixture). Only $T_m(\text{ice})$ and $T_m(\text{cla})$ were measured, ranging between -3.8 and -6.2 °C and between 7.9 and 11.3 °C, respectively. The latter microthermometry data imply that (i) the salinity is not equal to zero and (ii) there is a volatile component either made of pure CH_4 or of a gas mixture with unknown other component(s). In order to reconstruct the composition of the fluid inclusions with a complex gas mixture and where clathrate is present, the values of $T_m(\text{cla})$ and of the density of the volatile phase are required (Bakker, 1997). The two latter cases are typical examples illustrating some limitations of microthermometry analyses.

The selected natural FIs were also analyzed by Raman spectroscopy. Since all Raman calibration data were carried out at 22 – 32 °C, the P - V - X properties of the volatile part of FIs could be determined without the impact of the clathrate nucleation and dissociation, except a few particular cases where CH_4 clathrates could dissociate at up to 27 °C (Mullis, 1979; Sloan et al., 2007). Measurements were performed three times by focusing the laser on different places inside the FIs. For measuring $v_{\text{CH}_4}^*$ of CH_4 bearing FIs, a fused silica microcapillary (FSC) containing about 5 – 6 bars of CH_4 was analyzed before and after analyzing each FI (Fig. A.2 – Appendix D). The average values of the peak areas of gases were then used for the determination of composition using Equation 1 in Pasteris et al., (1988), with RRSCS of $\text{N}_2 = 1$ (by convention), RRSCS of $\text{CH}_4 = 7.73 \pm 0.16$ (this study) and RRSCS of $\text{CO}_2 = 2.29 \pm 0.04$ (Le et al., 2019). Once the composition of the fluid inclusion is determined, the relative variation of the peak positions of CH_4 ($v_{\text{CH}_4}^*$) and/or the CO_2 Fermi diad splitting (Δ) is used for the determination of pressure and density, using the appropriate calibration equation (from Equation 3 to 8). The uncertainty of the Raman results is the ultimate one calculated as described in section 3.3.3, whereas the uncertainty of microthermometry was determined from the uncertainty of the homogenization temperature (± 0.1 °C) and the graphic reading error (up to ± 1 °C) while using the VX diagrams of Thiéry et al. (1994).

Table 6 presents the comparison between the results obtained by Raman and microthermometry. Regarding sample Ta15, the composition of FIs determined from microthermometry data (93.8 – 96.5 mol% CH_4) is similar to that measured by Raman analyses (94.0 – 95.5 mol% CH_4). However, a noticeable difference in the measured pressure and density is observed (e.g., 899 – 942 bars and 0.353 – 0.366 g·cm $^{-3}$ for microthermometry measurements, compared to 736 – 784 bars and 0.338 – 0.347 g·cm $^{-3}$ for Raman measurements. The latter significant difference can be partially explained by the fact that the P - V properties of FIs of sample Ta15 greatly exceed the calibrated pressure (density)-range of our study (5 – 600 bars) (Table 6).

Regarding sample Mu618, the pressure and density determined by microthermometry and the composition (determined from Raman) using GERG-2004 EoS (319 – 632 bars and 0.242 – 0.370 g·cm $^{-3}$, respectively) are very close to the ones directly determined by Raman measurements. The difference in measured pressure and density are always less than 13 bars and 0.005 g·cm $^{-3}$,

670 respectively. The low density ($0.098 \text{ g}\cdot\text{cm}^{-3}$) of the bubble within FI Mu618.SQ-2.1 (Fig. 1c) made it
671 impossible to be characterized by microthermometry but it can be measured out by Raman analysis.

672 Regarding sample Mu1381, Raman and microthermometry results are overall in very good agreement.
673 The most significant difference in pressure and density noticed for FI Mu1381-2.2 are 35 bars ($\sim 8\%$)
674 and $0.014 \text{ g}\cdot\text{cm}^{-3}$ ($\sim 5\%$), respectively (Table 6).

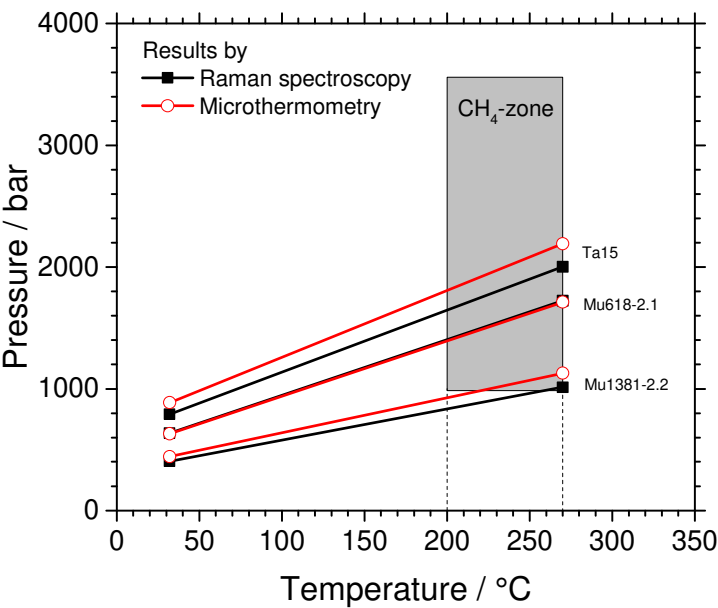
675 According to the study of Mullis et al. (1994), the trapping temperature of fluids within CH_4 -zone was
676 obtained from the homogenization of H_2O -rich FIs that is up to 270°C . The trapping pressure is
677 calculated within CH_4 -rich FIs at 270°C from the measured density. Here, we also used the GERG-
678 2004 EoS to calculate the trapping pressure and reported in Fig. 10 for comparison. With a small
679 difference of $0.005 \text{ g}\cdot\text{cm}^{-3}$ between the density obtained by Raman and microthermometry (IF Mu618-
680 2.1), the two relevant isochores are nearly identical. However, with a larger difference in density (e.g.,
681 a difference of $0.017 \text{ g}\cdot\text{cm}^{-3}$ for FI Ta15.1-2, and of $0.014 \text{ g}\cdot\text{cm}^{-3}$ for FI Mu1381-2.2), the isochores
682 slightly deviate by a difference of $\sim 100\text{--}200$ bars (around 10%) at 270°C (trapping temperature),
683 which however does not significantly change the geological interpretation (Table 6 and Fig. 10). The P -
684 V - X properties of the volatile part of FIs within PAN-V3 sample were determined from Raman
685 measurements only because of the complex composition and low density (Table 6). Thus, new
686 calibration data can provide P - V - X properties much faster than microthermometry measurements and
687 with a larger field of applicability.

688 Table 6: Comparison between Raman and microthermometry results. P_{Raman} and P_{Microth} are pressure (bar)
689 measured at 32°C . ρ_{Raman} is the density ($\text{g}\cdot\text{cm}^{-3}$) directly determined from Raman measurement and ρ_{Microth} is the
690 density calculated from microthermometry data using GERG-2004 EoS. $\Delta(P) = P_{\text{Raman}} - P_{\text{Microth}}$. $\Delta(\rho) = \rho_{\text{Raman}} -$
691 ρ_{Microth} . The uncertainty was provided for 1σ .

| N° IFs | Raman results | | | | | Microthermometry results | | Difference | | |
|--------------|------------------|----------|-----------------|--------------------|-------------------------------|--------------------------|-------------------------------|-------------|-------------------------------|--|
| | %CO ₂ | %CH 4 | %N ₂ | P_{Raman} | ρ_{Raman} | P_{Microth} | ρ_{Microth} | $\Delta(P)$ | $\Delta(\rho)$ | |
| | (mol%) | | | bar | $\text{g}\cdot\text{cm}^{-3}$ | bar | $\text{g}\cdot\text{cm}^{-3}$ | bar | $\text{g}\cdot\text{cm}^{-3}$ | |
| Ta15.1-2 | 6.0 | 94.0 | | 740 | 0.349 | 899 ± 8 | 0.366 ± 0.001 | 159 | 0.017 | |
| Ta15.1-6 | 4.5 | 95.5 | | 736 | 0.338 | 927 ± 9 | 0.353 ± 0.001 | 191 | 0.015 | |
| Ta15.1-7 | 4.5 | 95.5 | | 784 | 0.347 | 942 ± 8 | 0.354 ± 0.002 | 158 | 0.007 | |
| Mu618.SQ-1.1 | 13.4 | 86.6 | | 365 ± 8 | 0.296 ± 0.003 | 375 ± 11 | 0.300 ± 0.004 | 10 | 0.005 | |
| Mu618.SQ-2.1 | 16.7 | 83.3 | | 102 ± 7 | 0.098 ± 0.002 | - | - | - | - | |
| Mu618-2.1 | 13.5 | 86.5 | | 636 ± 10 | 0.371 ± 0.004 | 632 ± 11 | 0.370 ± 0.002 | -4 | -0.001 | |
| Mu618-2.2 | 9.8 | 90.2 | | 374 ± 8 | 0.281 ± 0.003 | 387 ± 12 | 0.286 ± 0.004 | 13 | 0.005 | |
| Mu1381-1.1 | | 69.1 | 30.9 | 344 ± 12 | 0.253 ± 0.004 | 319 ± 14 | 0.242 ± 0.005 | -25 | -0.011 | |
| Mu1381-1.2 | | 69.3 | 30.7 | 344 ± 12 | 0.252 ± 0.004 | 333 ± 14 | 0.248 ± 0.005 | -11 | -0.004 | |
| Mu1381-1.3 | | 69.1 | 30.9 | 342 ± 12 | 0.252 ± 0.004 | 348 ± 14 | 0.256 ± 0.005 | 6 | 0.004 | |
| Mu1381-2.2 | | 73.1 | 26.9 | 409 ± 13 | 0.275 ± 0.004 | 444 ± 13 | 0.289 ± 0.003 | 35 | 0.014 | |
| Mu1381-3.3 | | 72.7 | 27.3 | 458 ± 11 | 0.292 ± 0.004 | 449 ± 13 | 0.291 ± 0.003 | -9 | -0.001 | |

| | | | | | | | | | |
|------------|------|------|------|---------|---------------|---|---|---|---|
| PAN V3 A-1 | 40.6 | 22.6 | 36.8 | 103 ± 6 | 0.157 ± 0.003 | - | - | - | - |
| PAN V3 A-3 | 54.7 | 11.8 | 33.5 | 124 ± 7 | 0.232 ± 0.004 | - | - | - | - |
| PAN V3 D-1 | 63.0 | 13.5 | 23.5 | 102 ± 6 | 0.207 ± 0.003 | - | - | - | - |

692



693

694 Fig. 10. Isochores of FIs Mu618-2.1, Mu1381-2.2 and Ta15 calculated by GERG-2004 EoS. The grey area
695 represents the *PT* conditions of fluid entrapment within the CH₄-zone (Mullis, 1979; Mullis et al., 1994).

696 **4.3 Applicability of the calibration data to other laboratories**

697 The spectral features of CO₂ and CH₄ within the mixture of CO₂–CH₄ and CH₄–N₂ reported here show
698 similar behaviors as a function of pressure (density) and composition of gas mixtures, compared to the
699 results published by Seitz et al. (1993, 1996). However, Seitz and co-workers used a different
700 spectrometer with relatively low spectral resolution resulting in the scattering of their results. Also,
701 they did not study the variation of the Fermi diad splitting and did not specify the temperature of the
702 analyses (stated room temperature). Therefore, we represent only the comparison with the most recent
703 published calibration data using similar instruments (LabRAM HR, Horiba Jobin-Yvon) and
704 configurations (Table 7).

705 Table 7: Instrument and configurations of recent work for establishing calibration data for pure CO₂.

| | Laser (nm) | Gratings (grooves/mm) | Slit/hole | <i>T</i> (°C) | <i>P</i> (bar) | Peak position correction |
|------------------------|---------------|--------------------------|-----------|------------------|-------------------|-----------------------------|
| This study | 514 | 1800 | 200/1000 | 22 & 32 | 5-600 | No |
| Wang et al. (2019) | 532 & 514 | 1800 | 100/500 | 25 & 40 | 5-500 | Yes |
| Sublett et a. (2019) | 514 | 1800 | 150/400 | –160 to +450 | 10-500 | - |
| Lamadrid et al. (2017) | 514 | 1800 | 150/400 | 22-23 | < 60 | Yes |
| Fall et al. (2011) | 514 | 600/1800/2400 | 150/400 | –10 to 35 | 10-300 | No |

| | | | | | | |
|--------------------|-----|------|-------|----|--------|-----|
| Wang et al. (2011) | 532 | 1800 | - | 21 | 22-357 | Yes |
| Lin et al. (2007) | 514 | 1800 | 150/- | 22 | 1-600 | Yes |

706

707 Fig. 11a represents the comparison of the relationship between Δ and pressure of pure CO₂ obtained in
708 this work with previous studies. Since each published calibration data was made at a different
709 temperature, we observed a good agreement in the variation trend of Δ and the effect of temperature.
710 Indeed, the calibration curve was reasonably shifted to lower Fermi diad splitting with increasing
711 temperature, as noticed by Wang et al. (2011), Fall et al. (2011), Le et al. (2019), and Sublett et al.
712 (2019). We noticed that the departure of the calibration curve of Fall et al. (2011), Lamadrid et al.
713 (2017) and Sublett et al. (2019) differ from that of the calibration curves of Wang et al. (2011), Wang
714 et al. (2019), Le et al. (2019) and this study. That may indicate that there was a systematic error
715 causing a Δ -shift of about -0.1 cm^{-1} to the whole curves.

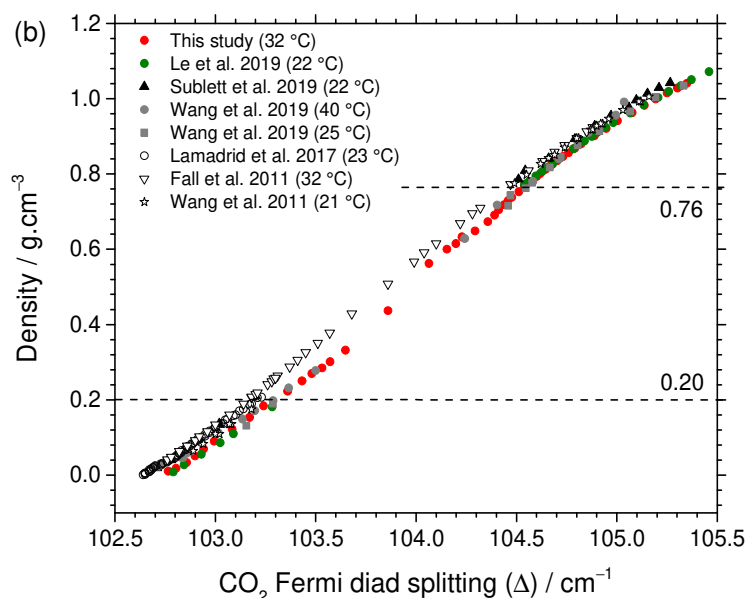
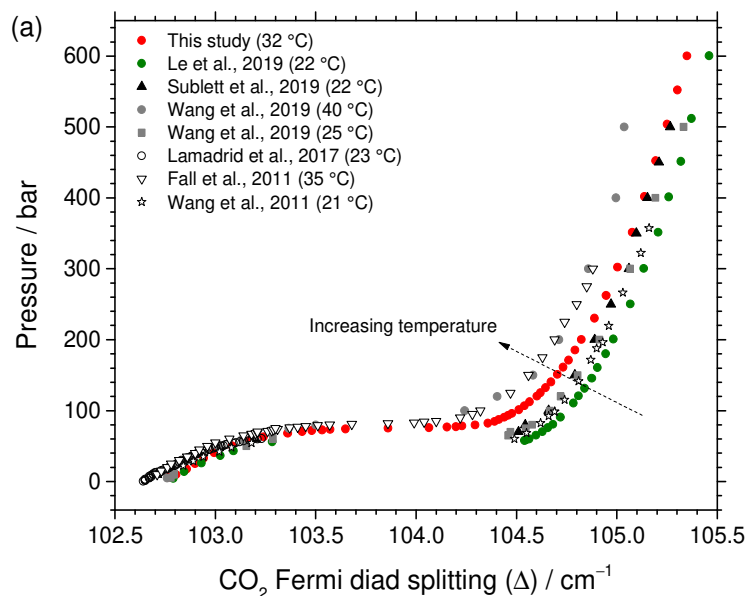


Fig. 11: Comparison of the relationship between Δ and (a) pressure or (b) density established at different temperatures and from different laboratories.

Fig. 11b represents the relationship between Δ and the density of pure CO₂ of this study, along with those of earlier studies. Our calibration is in excellent agreement with the whole experimental data by Wang et al. (2011) and Wang et al. (2019), and slightly different from those of Fall et al. (2011), Lamadrid et al. (2017) and Sublett et al. (2019) over high- (above ~ 0.76 g·cm⁻³) and low-density-range (under ~ 0.2 g·cm⁻³). The difference is always less than about 0.04 g·cm⁻³. The more pronounced discrepancy was observed over the middle density-range (~ 0.20 – 0.75 g·cm⁻³) with the difference of up to 0.1 g·cm⁻³. According to the study of Lamadrid et al. (2017), these discrepancies of calibration data may be due to the inconsistent procedure of the calibration of the Raman instruments, the wavelength correction method and also the systematic day-to-day errors (as seen in Fig. 11a,b). The significant difference in the middle density-range that was obtained at near critical point of CO₂ could be caused

by small fluctuation of pressure and temperature, different instrumentation, and/or by error in the use of different EoS in calculating density from pressure.

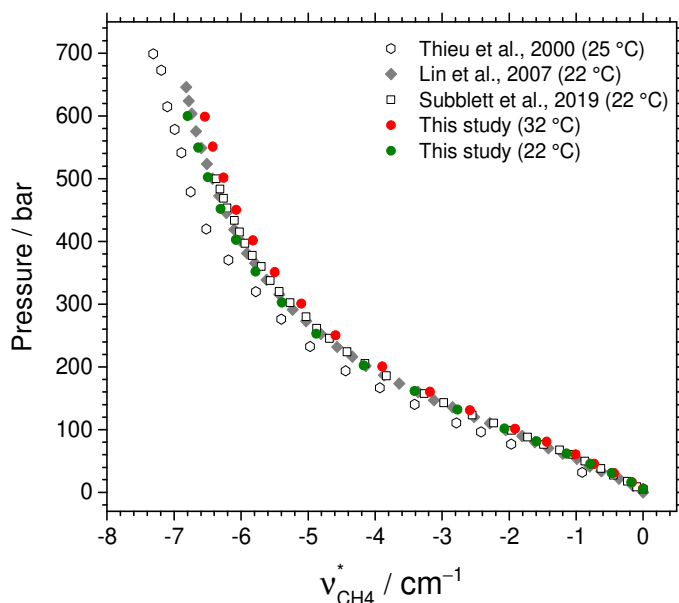


Fig. 12: Comparison of the variation of the downshift of the CH₄ peak position as a function of pressure and temperatures.

Fig. 12 shows a similar variation trend of $\nu_{\text{CH}_4}^*$ with pressure. With the consideration of temperature effect, our calibration curves obtained at 32 and 22 °C agree well with the published data obtained by Thieu et al. (2000) (at 25 °C), Lin et al. (2007) and Subblett et al. (2019) (at 22 °C). This proves the good reproducibility of the variation of the CH₄ band position for quantitative measurements. Overall, the applicability of the calibration data should be examined and corrected for each Raman instrument within different laboratories before being applied to the study of natural FIs. Even in the same laboratory, standards (natural/synthetic FIs or FSC) of known P - V - X properties should be regularly measured to prevent any variation or shifting of the instrumental responses.

5. Conclusions

Thanks to the use of an improved HPOC system, a system to prepare many gas mixtures at any composition at ~130 bars, and Raman spectroscopy, the relative Raman scattering cross-section of CH₄ (σ_{CH_4}) could be reevaluated within CH₄-N₂ mixtures of different compositions. It can be considered constant (7.73 ± 0.16) with the variation of pressure (density) and composition and so, used for the determination of the molar fraction (X) with an uncertainty of about ~0.5 mol%. Also, the Fermi diad splitting of CO₂ (Δ) and the relative variation of the peak position of CH₄ ($\nu_{\text{CH}_4}^*$) were demonstrated to be the most reliable spectral parameters with a satisfactory reproducibility for the monitoring of pressure and density (P - V) of CO₂-CH₄ and CH₄-N₂ mixtures. We also provided an interpretation of CH₄ peak position variation based on intermolecular interaction change using the Lennard-Jones 6-12 potential approximation. Several calibration polynomials fitted from our

experimental results were dedicatedly provided for each P - X range, linking pressure or density to the spectral parameters and the composition of the mixtures. Henceforth, the P - V - X properties of fluids containing binary or even ternary mixtures of CO_2 , CH_4 and N_2 gases (coupled with calibration data of Le et al. (2019)) can be directly determined from Raman spectra without any other complementary microthermometry analyses, making it a productive and accurate technique to quickly analyze FIs. Testing these calibration equations to natural FIs showed a good agreement with microthermometry data. It was noted that applying the calibration data reported in the present study may cause a higher uncertainty depending on the sensitivity of each Raman instrument, the instrumental calibration, and data processing protocol from one laboratory to another. Therefore, an examination and correction by analyzing standard samples are imperatively required before using any calibration data published in literature.

Acknowledgements

This paper is a part of the thesis of Van-Hoan Le (Université de Lorraine) who acknowledges the French Ministry of Education and Research and the ICEEL Institut Carnot. The work benefited financial support from CNRS-INSU CESSUR program.

Appendix A. Experimental protocol

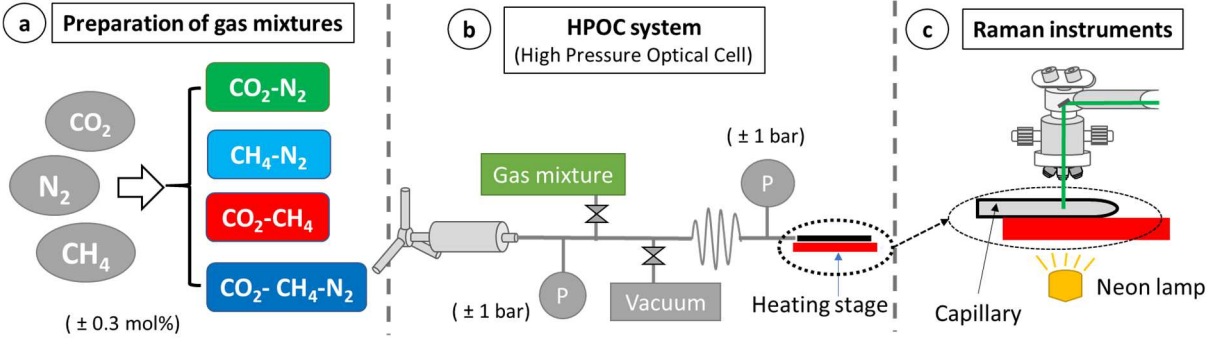


Fig. A.1. Scheme of the calibration strategy: (a) gas mixtures were prepared by a gas mixer and compressed (up to 130 bars) by a home-made pressurization system. It was then connected to (b) an HPOC system coupled with a transparent fused silica capillary (FSC) set on a Linkam CAP500 heating-cooling stage (± 0.1 °C). The HPOC system is composed of a manual pressure generator, two pressure transducers (± 1 bar), several valves, microtubes, and a pump to purge the system. (c) Raman in-situ analyzed of gas mixtures of known composition at controlled *PT* conditions. A neon lamp was set under the whole capillary and heating-cooling stage for wavelength correction.

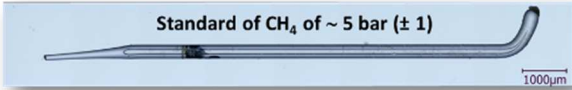


Fig. A.2. Photography of a sealed transparent microcapillary (called CH₄-standard) containing 5 ± 1 bar of CH₄ at room temperature. This standard was used for measuring $\nu_{CH_4}^*$ of CH₄ bearing within natural fluid inclusions (FIs). It was analyzed before and after analyzing every natural FIs for wavelength calibration of the spectrometer.

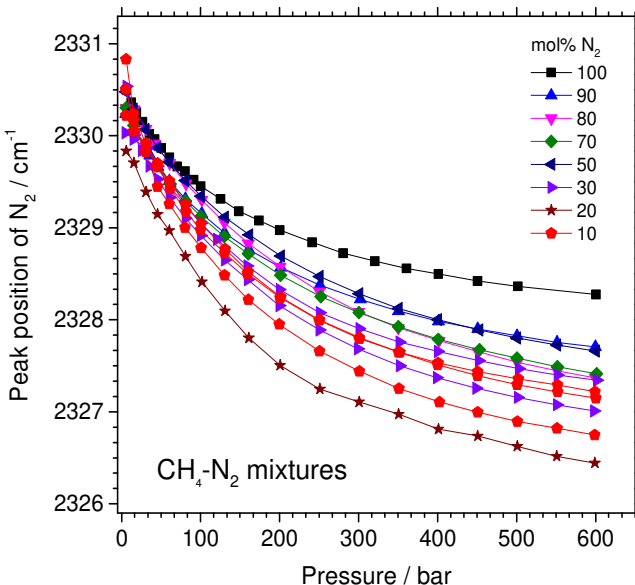


Fig. A.3. Variation of the fitted peak position of N₂ (corrected by a Ne line at ~2348.43 cm⁻¹) as a function of pressure and composition of CH₄–N₂ mixtures at 32 °C.

Appendix B. Calibration data of CO₂–CH₄ mixtures at 22 °C

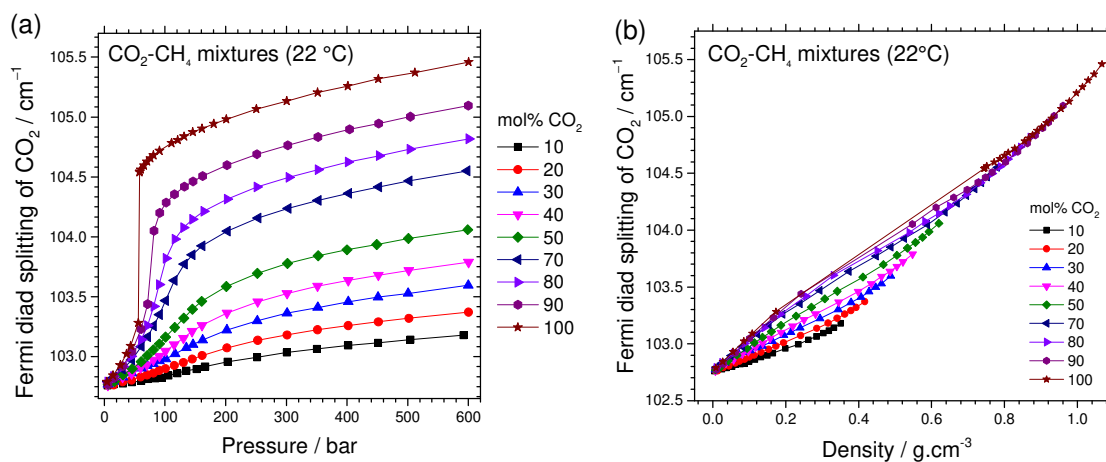


Fig. B.1. Variation of the Fermi diad splitting of CO₂ (Δ) as a function of pressure (a) or density (b) and composition of CO₂–CH₄ mixtures at 22 °C.

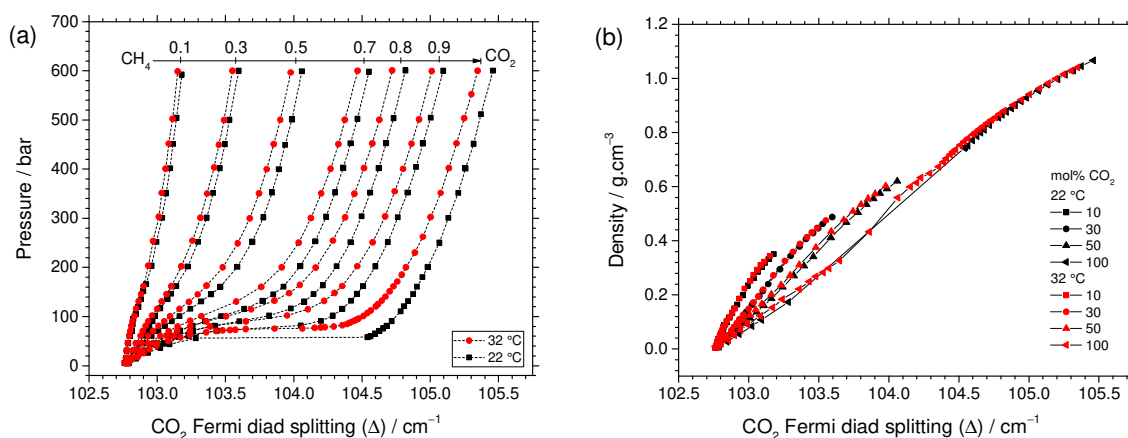


Fig. B.2. Comparison between the variation of the Fermi diad splitting of CO₂ as a function pressure (a) or density (b) and composition of CO₂–CH₄ mixtures obtained at 22 and 32 °C.

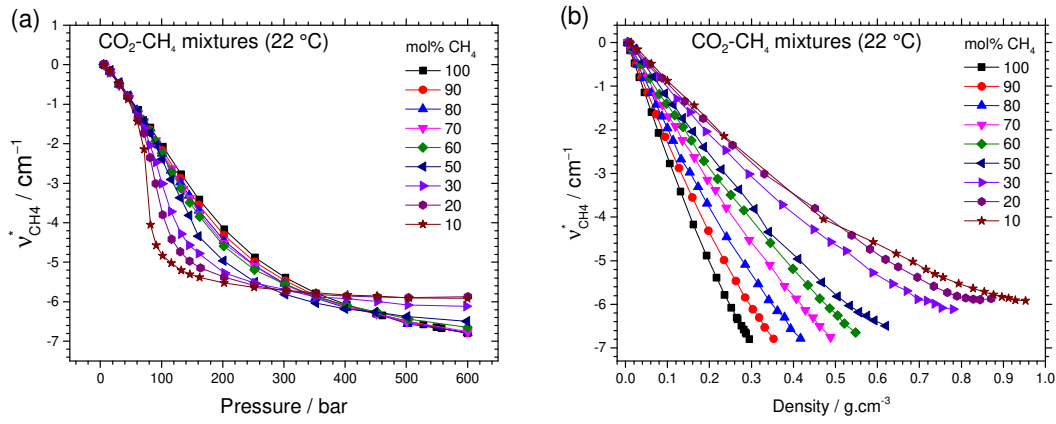


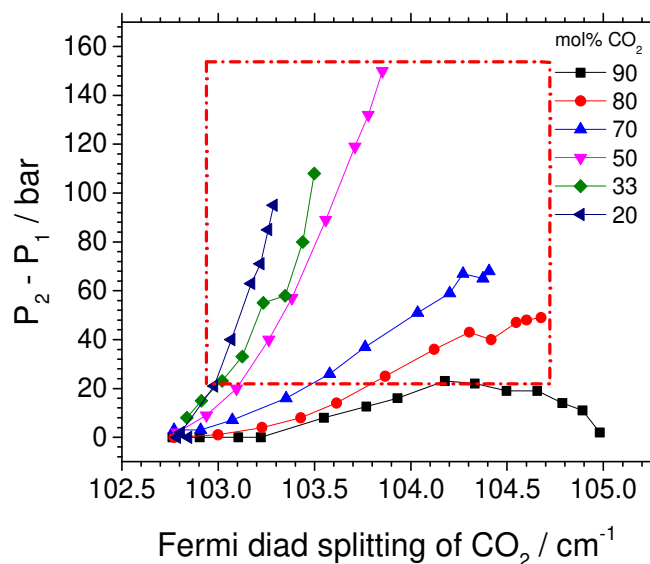
Fig. B.3. Relative variation of the fitted CH₄ peak position ($v_{CH_4}^*$) within CO₂-CH₄ mixtures as a function of composition (a) pressure or (b) density at 22 °C.

Appendix C. Statistical analyses for Raman calibration data of ternary gas mixtures

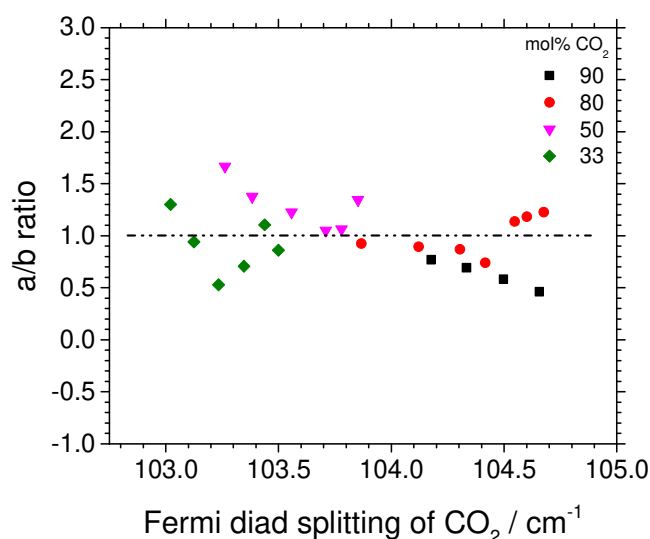
P_1 and P_2 is the “nominated” pressure determined from a given Δ value and molar proportion of CO₂ using the calibration equation of CO₂-CH₄ and CO₂-N₂ mixtures, respectively. Fig. C.1 represents the variation of the difference between P_2 and P_1 as a function of Δ and mixture composition. As shown in the insert in Fig. 8 and described in the section 3.3.2, the pressure (P) of the CO₂-CH₄-N₂ ternary mixtures can be deduced from the two “nominated” pressures P_1 and P_2 which are calculated from Δ and molar proportion of CO₂ using the calibration data set of two binary mixtures (CO₂-CH₄ and CO₂-N₂) if the a/b ratio is accurately known (a and b are described in the insert of Figure 8). The a/b ratio is calculated from experimental data by Eq. C.1 and reported in Fig. C.2. We assumed that the a/b ratio varies by a linear function of the molar fraction of CH₄ and N₂.

$$\frac{a}{b} = \frac{P - P_1}{P_2 - P} \quad (\text{Eq. C.1})$$

Because the uncertainty of the polynomial calibration equations of the binary gas mixtures ranges from ± 5 to ~ 20 bars (reported in section 3.3.1), we thus considered only the data points where the pressure difference ($P_2 - P_1$) is more than 20 bars (that were surrounded by the red frame in Fig. C.1). The pressure difference ($P_2 - P_1$) of the points outside the red frame (< 20 bars) is therefore negligible. Statistical analyses give the average value of the a/b ratio = $0.98 \pm 0.06 \approx 1$ that validated our assumption of the linear correlation between the molar fraction of N₂ and CH₄ (within ternary mixtures) in the determination of pressure P from P_1 and P_2 (Fig. C.2). Therefore, a and b are reasonably the molar proportion of CH₄ and N₂ in ternary mixtures, respectively. The pressure and the density of ternary mixtures of any concentration can be henceforth determined from the molar concentration and the Fermi diad splitting of CO₂ using the calibration equations of CO₂-CH₄ (this study) and CO₂-N₂ (Le et al., 2019) mixtures (Equation 8).



818
 819 Fig. C.1. Difference between the “nominated” pressure of CO₂–CH₄ and CO₂–N₂ mixtures ($P_2 - P_1$) at
 820 given Δ value and CO₂ concentration. According to the uncertainty reported for regression polynomial
 821 calibration equation, the difference of ($P_2 - P_1$) that is less than about 20 bars is negligible.



822
 823 Fig. C.2. Variation of the a/b ratios as a function of Δ and composition of gas mixtures. Statistical
 824 analyses give the averaged value of the a/b ratio = 0.98 ~ 1 while the molar proportions of CH₄ and N₂
 825 in the ternary mixture are equal.

Appendix D. Interpretation of the peak shift as a function of intermolecular interaction

Table D.1: Density ($\text{g}\cdot\text{cm}^{-3}$ or molecular number. cm^{-3}) and intermolecular separation r (\AA) of CH_4 molecules calculated for a given pressure (bar). The intermolecular separation r at a given pressure (or given density) is calculated by assuming that every molecule is separated by the same distance.

| Pressure | Density | Density | Intermolecular distance (r) |
|----------|-----------------------------------|--|-----------------------------|
| (bar) | ($\text{g}\cdot\text{cm}^{-3}$) | (Molecule number. cm^{-3}) $\cdot 10^{21}$ | \AA |
| 15 | 0.010 | 0.37 | 14.0 |
| 30 | 0.020 | 0.75 | 11.0 |
| 90 | 0.065 | 2.45 | 7.4 |
| 130 | 0.097 | 3.67 | 6.5 |
| 200 | 0.150 | 5.66 | 5.6 |
| 300 | 0.206 | 7.74 | 5.1 |
| 400 | 0.242 | 9.10 | 4.8 |
| 500 | 0.267 | 10.06 | 4.6 |
| 600 | 0.287 | 10.80 | 4.5 |
| 1200 | 0.355 | 13.37 | 4.2 |
| 1400 | 0.370 | 13.92 | 4.2 |
| 1600 | 0.382 | 14.39 | 4.1 |

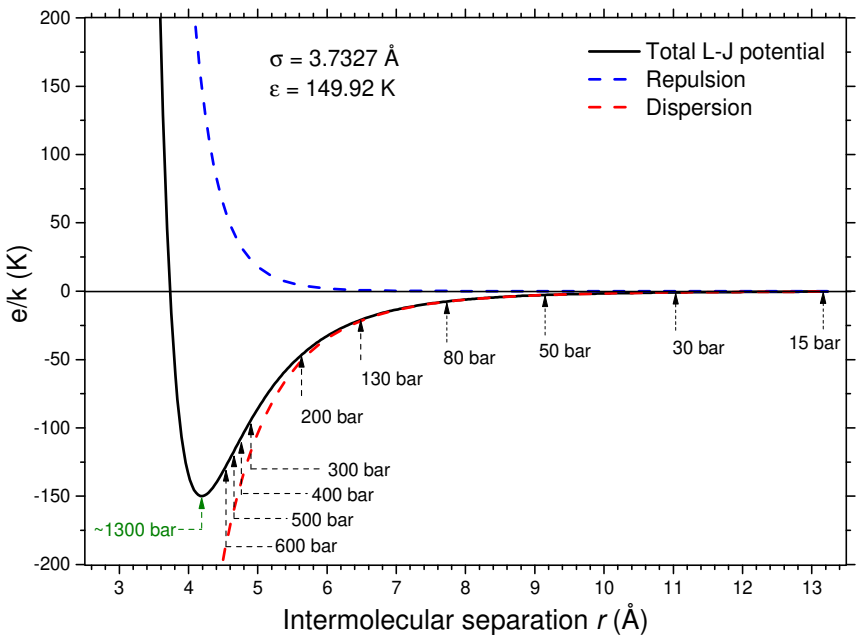


Fig. D.1. Black-solid line: the variation of Lennard-Jones 6-12 potential of pure CH_4 as a function of intermolecular separation r . The total potential energy (solid-black line) is the sum of energy coming

835 from repulsive (blue-dashed line) and attractive forces (red-dashed line) experienced between
836 molecules. Lennard-Jones parameters (σ , ϵ) of CH₄ are from Möller et al. (1992).

References

- Akinfiyev, N.N., Diamond, L.W., 2010. Thermodynamic model of aqueous CO₂–H₂O–NaCl solutions from –22 to 100°C and from 0.1 to 100MPa. *Fluid Phase Equilibria* 295, 104–124. <https://doi.org/10.1016/j.fluid.2010.04.007>
- Amat, G., Pimbert, M., 1965. On Fermi resonance in carbon dioxide. *J. Mol. Spectrosc.* 16, 278–290. [https://doi.org/10.1016/0022-2852\(65\)90123-2](https://doi.org/10.1016/0022-2852(65)90123-2)
- Angus, S., Armstrong, B., De Reuck, K.M., Altunin, V.V., Gadetskii, O.G., Chapela, G.A., Rowlinson, J.S., 1976. International thermodynamic tables of the fluid state. Carbon Dioxide 3, 338–342.
- Angus, S., Reuck, K.M. de, Armstrong, B., 1979. International thermodynamic tables of the fluid state - 6; nitrogen. Oxford : Pergamon Press.
- Bakker, R.J., 1997. Clathrates: Computer programs to calculate fluid inclusion V-X properties using clathrate melting temperatures. *Comput. Geosci.* 23, 1–18. [https://doi.org/10.1016/S0098-3004\(96\)00073-8](https://doi.org/10.1016/S0098-3004(96)00073-8)
- Bakker, R.J., Diamond, L.W., 2000. Determination of the composition and molar volume of H₂O–CO₂ fluid inclusions by microthermometry. *Geochim. Cosmochim. Acta* 64, 1753–1764. [https://doi.org/10.1016/S0016-7037\(99\)00334-8](https://doi.org/10.1016/S0016-7037(99)00334-8)
- Ben-Amotz, D., LaPlant, F., Shea, D., Gardecki, J., List, D., 1992. Raman Studies of Molecular Potential Energy Surface Changes in Supercritical Fluids, in: *Supercritical Fluid Technology*, ACS Symposium Series. American Chemical Society, pp. 18–30. <https://doi.org/10.1021/bk-1992-0488.ch002>
- Benson, S.M., Cole, D.R., 2008. CO₂ Sequestration in Deep Sedimentary Formations. *Elements* 4, 325–331. <https://doi.org/10.2113/gselements.4.5.325>
- Bertrán, J.F., 1983. Study of the Fermi doublet v₁ — 2v₂ in the Raman spectra of CO₂ in different phases. *Spectrochim. Acta Part Mol. Spectrosc.* 39, 119–121. [https://doi.org/10.1016/0584-8539\(83\)80066-X](https://doi.org/10.1016/0584-8539(83)80066-X)
- Bodnar, R.J., Lecumberri-Sanchez, P., Moncada, D., Steele-MacInnis, M., 2014. 13.5 - Fluid Inclusions in Hydrothermal Ore Deposits, in: Holland, H.D., Turekian, K.K. (Eds.), *Treatise on Geochemistry* (Second Edition). Elsevier, Oxford, pp. 119–142. <https://doi.org/10.1016/B978-0-08-095975-7.01105-0>
- Burke, E.A.J., 2001. Raman microspectrometry of fluid inclusions. *Lithos, Fluid Inclusions: Phase Relationships - Methods - Applications. A Special Issue in honour of Jacques Touret* 55, 139–158. [https://doi.org/10.1016/S0024-4937\(00\)00043-8](https://doi.org/10.1016/S0024-4937(00)00043-8)
- Burruss, R.C., 1981. Analysis of fluid inclusions; phase equilibria at constant volume. *Am. J. Sci.* 281, 1104–1126. <https://doi.org/10.2475/ajs.281.8.1104>
- Carocci, E., Marignac, C., Cathelineau, M., Truche, L., Lecomte, A., Pinto, F., 2019. Rutile from Panasqueira (Central Portugal): An Excellent Pathfinder for Wolframite Deposition. *Minerals* 9, 9. <https://doi.org/10.3390/min9010009>
- Cathelineau, M., Marignac, C., Marignac, L.-M., Boiron, M.-C., Dejean, M., Carocci, E., 2017. Are we sure to know the fluids responsible for W mineralization at Panasqueira (Portugal): the case for loss of information due to intense quartz recrystallization and FI natural decrepitation. *ECROFI* 98.
- Caumon, M.-C., Dubessy, J., Robert, P., Tarantola, A., 2013. Fused-silica capillary capsules (FSCCs) as reference synthetic aqueous fluid inclusions to determine chlorinity by Raman spectroscopy. *Eur. J. Mineral.* 25, 755–763. <https://doi.org/DOI: 10.1127/0935-1221/2013/0025-2280>
- Caumon, M.-C., Robert, P., Laverret, E., Tarantola, A., Randi, A., Pironon, J., Dubessy, J., Girard, J.-P., 2014. Determination of methane content in NaCl–H₂O fluid inclusions by Raman spectroscopy. Calibration and application to the external part of the Central Alps (Switzerland). *Chem. Geol.* 378, 52–61. <https://doi.org/10.1016/j.chemgeo.2014.03.016>
- Caumon, M.-C., Tarantola, A., Wang, W., 2019. Raman spectra of gas mixtures in fluid inclusions: Effect of quartz birefringence on composition measurement. *J. Raman Spectrosc.* 0. <https://doi.org/10.1002/jrs.5605>
- Charlou, J.L., Donval, J.P., Fouquet, Y., Jean-Baptiste, P., Holm, N., 2002. Geochemistry of high H₂ and CH₄ vent fluids issuing from ultramafic rocks at the Rainbow hydrothermal field (36°14'N, MAR). *Chem. Geol.* 191, 345–359. [https://doi.org/10.1016/S0009-2541\(02\)00134-1](https://doi.org/10.1016/S0009-2541(02)00134-1)

- Chi, G., Chou, I.-M., Lu, H., 2003. An overview on current fluid-inclusions research and applications. *Acta Petrol. Sin.* 19, 201–212.
- Chou, I.-M., Burruss, R.C., Lu, W., 2005. Chapter 24 - A new optical capillary cell for spectroscopic studies of geologic fluids at pressures up to 100 MPa, in: Chen, J., Wang, Y., Duffy, T.S., Shen, G., Dobrzynetska, L.F. (Eds.), *Advances in High-Pressure Technology for Geophysical Applications*. Elsevier, Amsterdam, pp. 475–485. <https://doi.org/10.1016/B978-044451979-5.50026-0>
- Chou, I.-M., Pasteris, J.D., Seitz, J.C., 1990. High-density volatiles in the system C-O-H-N for the calibration of a laser Raman microprobe. *Geochim. Cosmochim. Acta* 54, 535–543. [https://doi.org/10.1016/0016-7037\(90\)90350-T](https://doi.org/10.1016/0016-7037(90)90350-T)
- Chou, I.-M., Song, Y., Burruss, R.C., 2008. A new method for synthesizing fluid inclusions in fused silica capillaries containing organic and inorganic material. *Geochim. Cosmochim. Acta* 72, 5217–5231. <https://doi.org/10.1016/j.gca.2008.07.030>
- Collins, P.L.F., 1979. Gas hydrates in CO₂-bearing fluid inclusions and the use of freezing data for estimation of salinity. *Econ. Geol.* 74, 1435–1444. <https://doi.org/10.2113/gsecongeo.74.6.1435>
- Diamond, L.W., 1994. Salinity of multivolatile fluid inclusions determined from clathrate hydrate stability. *Geochim. Cosmochim. Acta* 58, 19–41. [https://doi.org/10.1016/0016-7037\(94\)90443-X](https://doi.org/10.1016/0016-7037(94)90443-X)
- Diamond, L.W., 1992. Stability of CO₂ clathrate hydrate + CO₂ liquid + CO₂ vapour + aqueous KCl-NaCl solutions: Experimental determination and application to salinity estimates of fluid inclusions *. *Geochim. Cosmochim. Acta* 56, 273–280. [https://doi.org/10.1016/0016-7037\(92\)90132-3](https://doi.org/10.1016/0016-7037(92)90132-3)
- Diamond, L.W., 1990. Fluid inclusion evidence for P-V-T-X evolution of hydrothermal solutions in late-Alpine gold-quartz veins at Brusson, Val d'Ayas, Northwest Italian Alps. *Am. J. Sci.* 912–958. <https://doi.org/10.2475/ajs.290.8.912>
- Dubessy, J., Caumon, M.-C., Rull, F., 2012. Instrumentation in Raman spectroscopy: elementary theory and practice. *EMU Notes Mineral.* 12, 83–172. <https://doi.org/10.1180/EMU-notes.12.3>
- Dubessy, J., Poty, B., Ramboz, C., 1989. Advances in C-O-H-N-S fluid geochemistry based on micro-Raman spectrometric analysis of fluid inclusions. *Eur. J. Mineral.* 517–534. <https://doi.org/10.1127/ejm/1/4/0517>
- Duschek, W., Kleinrahm, R., Wagner, W., 1990. Measurement and correlation of the (pressure, density, temperature) relation of carbon dioxide II. Saturated-liquid and saturated-vapour densities and the vapour pressure along the entire coexistence curve. *J. Chem. Thermodyn.* 22, 841–864. [https://doi.org/10.1016/0021-9614\(90\)90173-N](https://doi.org/10.1016/0021-9614(90)90173-N)
- Eckhardt, G., Wagner, W.G., 1966. On the calculation of absolute Raman scattering cross sections from Raman scattering coefficients. *J. Mol. Spectrosc.* 19, 407–411. [https://doi.org/10.1016/0022-2852\(66\)90262-1](https://doi.org/10.1016/0022-2852(66)90262-1)
- Etheridge, M.A., Wall, V.J., Vernon, R.H., 1983. The role of the fluid phase during regional metamorphism and deformation. *J. Metamorph. Geol.* 1, 205–226. <https://doi.org/10.1111/j.1525-1314.1983.tb00272.x>
- Fabre, D., Oksengorn, B., 1992. Pressure and Density Dependence of the CH₄ and N₂ Raman Lines in an Equimolar CH₄/N₂ Gas Mixture. *Appl. Spectrosc.* 46, 468–471.
- Fall, A., Eichhubl, P., Cumella, S.P., Bodnar, R.J., Laubach, S.E., Becker, S.P., 2012. Testing the basin-centered gas accumulation model using fluid inclusion observations: Southern Piceance Basin, Colorado Basin-Centered Gas Accumulation, Piceance Basin, Colorado. *AAPG Bull.* 96, 2297–2318. <https://doi.org/10.1306/05171211149>
- Fall, A., Tattitch, B., Bodnar, R.J., 2011. Combined microthermometric and Raman spectroscopic technique to determine the salinity of H₂O–CO₂–NaCl fluid inclusions based on clathrate melting. *Geochim. Cosmochim. Acta* 75, 951–964. <https://doi.org/10.1016/j.gca.2010.11.021>
- Fang, J., Chou, I.-M., Chen, Y., 2018. Quantitative Raman spectroscopic study of the H₂–CH₄ gaseous system. *J. Raman Spectrosc.* 49, 710–720. <https://doi.org/10.1002/jrs.5337>
- Fermi, E., 1931. Über den Ramaneffekt des Kohlendioxyds. *Z. Für Phys.* 71, 250–259. <https://doi.org/10.1007/BF01341712>
- Fouche, D.G., Chang, R.K., 1971. Relative raman cross section for n₂, o₂, co, co₂, so₂, and h₂s. *Appl. Phys. Lett.* 18, 579–580. <https://doi.org/10.1063/1.1653548>

- 950 Frey, M., Teichmüller, M., Teichmüller, R., Mullis, J., Künzi, B., Breitschmid, A., 1980. Very low-
951 grade metamorphism in external parts of the Central Alps: Illite crystallinity, coal rank and
952 fluid inclusion data. *Eclogae Geol Helvetiae* 73, 173–203.
- 953 Frezzotti, M.L., Tecce, F., Casagli, A., 2012. Raman spectroscopy for fluid inclusion analysis. *J.*
954 *Geochem. Explor.* 112, 1–20. <https://doi.org/10.1016/j.gexplo.2011.09.009>
- 955 Fyfe, W.S., Thompson, A.B., Price, N.J., 1978. Fluids in the earth's crust : their significance in
956 metamorphic, tectonic, and chemical transport processes. Amsterdam ; New York : Elsevier
957 Scientific ; New York : distributions for the U.S. and Canada, Elsevier/North-Holland.
- 958 Garcia-Baonza, V., Rull, F., Dubessy, J., 2012. Raman Spectroscopy of Gases, Water and other
959 Geological Fluids, in: Ferraris, G., Dubessy, J., Caumon, M.-C., Rull, F. (Eds.), *Raman*
960 *Spectroscopy Applied to Earth Sciences and Cultural Heritage*. European Mineralogical
961 Union, pp. 279–320. <https://doi.org/10.1180/EMU-notes.12.8>
- 962 Garrabos, Y., Chandrasekharan, V., Echargui, M.A., Marsault-Herail, F., 1989. Density effect on the
963 raman fermi resonance in the fluid phases of CO₂. *Chem. Phys. Lett.* 160, 250–256.
964 [https://doi.org/10.1016/0009-2614\(89\)87591-8](https://doi.org/10.1016/0009-2614(89)87591-8)
- 965 Garrabos, Y., Tufeu, R., Le Neindre, B., Zalczer, G., Beysens, D., 1980. Rayleigh and Raman
966 scattering near the critical point of carbon dioxide. *J. Chem. Phys.* 72, 4637–4651.
967 <https://doi.org/10.1063/1.439706>
- 968 Hacura, A., 1997. High pressure Raman study of Fermi resonance in CO₂ in gaseous CO₂–N₂
969 mixtures. *Phys. Lett. A* 227, 237–240. [https://doi.org/10.1016/S0375-9601\(97\)00010-8](https://doi.org/10.1016/S0375-9601(97)00010-8)
- 970 Hollister, L.S., Burruss, R.C., 1976. Phase equilibria in fluid inclusions from the Khtada Lake
971 metamorphic complex. *Geochim. Cosmochim. Acta* 40, 163–175.
972 [https://doi.org/10.1016/0016-7037\(76\)90174-5](https://doi.org/10.1016/0016-7037(76)90174-5)
- 973 Howard-Lock, H.E., Stoicheff, B.P., 1971. Raman intensity measurements of the Fermi diad v₁, 2v₂ in
974 12CO₂ and 13CO₂. *J. Mol. Spectrosc.* 37, 321–326. [https://doi.org/10.1016/0022-](https://doi.org/10.1016/0022-2852(71)90302-X)
975 [2852\(71\)90302-X](https://doi.org/10.1016/0022-2852(71)90302-X)
- 976 Huang, Y., Tarantola, A., Wang, W., Caumon, M.-C., Pironon, J., Lu, W., Yan, D., Zhuang, X., 2018.
977 Charge history of CO₂ in Lishui sag, East China Sea basin: Evidence from quantitative
978 Raman analysis of CO₂-bearing fluid inclusions. *Mar. Pet. Geol.* 98, 50–65.
979 <https://doi.org/10.1016/j.marpetgeo.2018.07.030>
- 980 Hurai, V., Huraiova, M., Slobodnik, M., Thomas, R., 2015. Geofluids: Developments in
981 Microthermometry, Spectroscopy, Thermodynamics, and stable isotopes.
- 982 Jones, J.E., Chapman, S., 1924. On the determination of molecular fields. —II. From the equation of
983 state of a gas. *Proc. R. Soc. Lond. Ser. Contain. Pap. Math. Phys. Character* 106, 463–477.
984 <https://doi.org/10.1098/rspa.1924.0082>
- 985 Kawakami, Y., Yamamoto, J., Kagi, H., 2003. Micro-Raman Densimeter for CO₂ Inclusions in
986 Mantle-Derived Minerals. *Appl. Spectrosc.* 57, 1333–1339.
- 987 Kelley, D.S., 1996. Methane-rich fluids in the oceanic crust. *J. Geophys. Res. Solid Earth* 101, 2943–
988 2962. <https://doi.org/10.1029/95JB02252>
- 989 Kramida, A., Ralchenko, Y., Reader, J., NIST ASD Team, 2018. NIST Atomic Spectra Database
990 (version 5.6.1).
- 991 Kunz, O. (Ed.), 2007. The GERG-2004 wide-range equation of state for natural gases and other
992 mixtures, *Als Ms. gedr. ed, Fortschritt-Berichte VDI Reihe 6, Energietechnik*. VDI-Verl,
993 Düsseldorf.
- 994 Lamadrid, H.M., Moore, L.R., Moncada, D., Rimstidt, J.D., Burruss, R.C., Bodnar, R.J., 2017.
995 Reassessment of the Raman CO₂ densimeter. *Chem. Geol.* 450, 210–222.
996 <https://doi.org/10.1016/j.chemgeo.2016.12.034>
- 997 Lamadrid, H.M., Steele-Macinnis, M., Bodnar, R., 2018. Relationship between Raman spectral
998 features and fugacity in mixtures of gases. *J. Raman Spectrosc.*
999 <https://doi.org/10.1002/jrs.5304>
- 1000 Lammers, L.N., Brown, G.E., Bird, D.K., Thomas, R.B., Johnson, N.C., Rosenbauer, R.J., Maher, K.,
1001 2015. Sedimentary reservoir oxidation during geologic CO₂ sequestration. *Geochim.*
1002 *Cosmochim. Acta* 155, 30–46. <https://doi.org/10.1016/j.gca.2015.02.001>
- 1003 Le, V.-H., Caumon, M.-C., Tarantola, A., Randi, A., Robert, P., Mullis, J., 2019. Quantitative
1004 Measurements of Composition, Pressure, and Density of Microvolumes of CO₂–N₂ Gas
1005 Mixtures by Raman Spectroscopy. *Anal. Chem.* 91, 14359–14367.
1006 <https://doi.org/10.1021/acs.analchem.9b02803>

- Lee, B.I., Kesler, M.G., 1975. A generalized thermodynamic correlation based on three-parameter corresponding states. *AIChE J.* 21, 510–527. <https://doi.org/10.1002/aic.690210313>
- Lemmon, E.W., Huber, M.L., McLinden, M.O., 2013. NIST Standard Reference Database 23: Reference Fluid Thermodynamic and Transport Properties-REFPROP, Version 9.1, National Institute of Standards and Technology, Stand. Ref. Data Program Gaithersburg.
- Lin, Bodnar, R.J., Becker, S.P., 2007. Experimental determination of the Raman CH₄ symmetric stretching (ν₁) band position from 1–650bar and 0.3–22°C: Application to fluid inclusion studies. *Geochim. Cosmochim. Acta* 71, 3746–3756. <https://doi.org/10.1016/j.gca.2007.05.016>
- Lin, F., Sum, A.K., Bodnar, R.J., 2007. Correlation of methane Raman ν₁ band position with fluid density and interactions at the molecular level. *J. Raman Spectrosc.* 38, 1510–1515. <https://doi.org/10.1002/jrs.1804>
- Lu, W., Chou, I.-M., Burruss, R.C., Song, Y., 2007. A unified equation for calculating methane vapor pressures in the CH₄–H₂O system with measured Raman shifts. *Geochim. Cosmochim. Acta* 71, 3969–3978. <https://doi.org/10.1016/j.gca.2007.06.004>
- Möller, D., Oprzynski, J., Müller, A., Fischer, J., 1992. Prediction of thermodynamic properties of fluid mixtures by molecular dynamics simulations: methane-ethane. *Mol. Phys.* 75, 363–378. <https://doi.org/10.1080/00268979200100291>
- Mullis, J., 1987. Fluid inclusion studies during very-low grade metamorphism. Frey M Ed Low Temp. Metamorph. Blackie 162–199.
- Mullis, J., 1979. The system methane-water as a geological thermometer and barometer from the external part of the Central Alps. *Bull. Minéral.* 102, 526–536.
- Mullis, J., 1975. Growth conditions of quartz crystals from the Val d’Iliez (Valais, Switzerland). *Schweiz Min Petr Mitt* 55, 419–430.
- Mullis, J., Dubessy, J., Poty, B., O’Neil, J., 1994. Fluid regimes during late stages of a continental collision: Physical, chemical, and stable isotope measurements of fluid inclusions in fissure quartz from a geotraverse through the Central Alps, Switzerland. *Geochim. Cosmochim. Acta* 58, 2239–2267. [https://doi.org/10.1016/0016-7037\(94\)90008-6](https://doi.org/10.1016/0016-7037(94)90008-6)
- Musso, M., Matthai, F., Keutel, D., Oehme, K.-L., 2004. Critical Raman line shape behavior of fluid nitrogen. *Pure Appl. Chem.* 76, 147–155. <https://doi.org/10.1351/pac200476010147>
- Musso, M., Matthai, F., Keutel, D., Oehme, K.-L., 2002. Isotropic Raman line shapes near gas–liquid critical points: The shift, width, and asymmetry of coupled and uncoupled states of fluid nitrogen. *J. Chem. Phys.* 116, 8015–8027. <https://doi.org/10.1063/1.1468885>
- Noronha, F., Doria, A., Dubessy, J., Charoy, B., 1992. Characterization and timing of the different types of fluids present in the barren and ore-veins of the W-Sn deposit of Panasqueira, Central Portugal. *Miner. Deposita* 27, 72–79. <https://doi.org/10.1007/BF00196084>
- Pasteris, J.D., Wopenka, B., Seitz, J.C., 1988. Practical aspects of quantitative laser Raman microprobe spectroscopy for the study of fluid inclusions. *Geochim. Cosmochim. Acta* 52, 979–988. [https://doi.org/10.1016/0016-7037\(88\)90253-0](https://doi.org/10.1016/0016-7037(88)90253-0)
- Penney, Goldman, Lapp, 1972. Raman Scattering Cross Sections. *Nat. Phys. Sci.* 235, 110–112.
- Placzek, G., 1934. Rayleigh-Streuung und Raman-Effekt. Akad. Verlag-Ges.
- Poty, B.P., 1967. La croissance des cristaux de quartz dans le filons sur l’exemple du filon de La Gardette (Bourg d’Oisans) et des filons du massif du Mont-Blanc (phdthesis). Université de Nancy.
- Poty, B.P., Stalder, H.-A., Weisbrod, A.M., 1974. Fluid inclusion studies in quartz from fissures of western and central Alps. *Schweiz Min Petr Mitt* 54, 54.
- Roedder, E., 1984. Fluid Inclusions. *Reviews in Mineralogy. Mineral. Soc. Am.* 12, 644.
- Roedder, E., 1979. Fluid inclusions as samples of ore fluids. *Geochem. Hydrothermal Ore Depos.* 684–737.
- Roedder, E., Bodnar, R.J., 1997. Fluid inclusion studies of hydrothermal ore deposits. *Geochem. Hydrothermal Ore Depos.* 657–698.
- Rosso, K.M., Bodnar, R.J., 1995. Microthermometric and Raman spectroscopic detection limits of CO₂ in fluid inclusions and the Raman spectroscopic characterization of CO₂. *Geochim. Cosmochim. Acta* 59, 3961–3975. [https://doi.org/10.1016/0016-7037\(95\)94441-H](https://doi.org/10.1016/0016-7037(95)94441-H)
- Schneider, G.M., 1979. Methane–International Thermodynamic Tables of the Fluid State, Bd. 5. Von S. Angus, B. Armstrong and K. M. de Reuck. Pergamon Press, Oxford–New York 1978. 1.

Aufl., XXIV, 251 S., zahlr. Abb. u. Tab., geb. \$ 38,00. Chem. Ing. Tech. 51, 766–766.
<https://doi.org/10.1002/cite.330510728>
 Schrötter, H.W., Klöckner, 1979. Raman Scattering Cross Section in Gases and Liquids, in: Topics in
 Current Physics. pp. 123–164.
 Seitz, J.C., Pasteris, J.D., Chou, I.-M., 1996. Raman spectroscopic characterization of gas mixtures. II.
 Quantitative composition and pressure determination of the CO₂-CH₄ system. Am. J. Sci.
 296, 577–600.
 Seitz, J.C., Pasteris, J.D., Chou, I.-M., 1993. Raman spectroscopic characterization of gas mixtures; I,
 Quantitative composition and pressure determination of CH₄, N₂ and their mixtures. Am. J.
 Sci. 293, 297–321.
 Sloan, E.D., Koh, C.A., Koh, C., 2007. Clathrate Hydrates of Natural Gases. CRC Press.
 Soave, G., 1972. Equilibrium constants from a modified Redlich-Kwong equation of state. Chem. Eng.
 Sci. 27, 1197–1203. [https://doi.org/10.1016/0009-2509\(72\)80096-4](https://doi.org/10.1016/0009-2509(72)80096-4)
 Song, Y., Chou, I., Hu, W., Robert, B., Lu, W., 2009. CO₂ Density-Raman Shift Relation Derived
 from Synthetic Inclusions in Fused Silica Capillaries and Its Application. Acta Geol. Sin. -
 Engl. Ed. 83, 932–938. <https://doi.org/10.1111/j.1755-6724.2009.00090.x>
 Sublett, D.M., Sendula, E., Lamadrid, H., Steele-MacInnis, M., Spiekermann, G., Burruss, R.C.,
 Bodnar, R.J., 2019. Shift in the Raman symmetric stretching band of N₂, CO₂, and CH₄ as a
 function of temperature, pressure, and density. J. Raman Spectrosc. n/a.
<https://doi.org/10.1002/jrs.5805>
 Tarantola, A., Mullis, J., Vennemann, T., Dubessy, J., de Capitani, C., 2007. Oxidation of methane at
 the CH₄/H₂O–(CO₂) transition zone in the external part of the Central Alps, Switzerland:
 Evidence from stable isotope investigations. Chem. Geol., New Results in Fluid and Melt
 Inclusion Research 237, 329–357. <https://doi.org/10.1016/j.chemgeo.2006.07.007>
 Thiéry, R., Kerkhof, A., Dubessy, J., 1994. v_X properties of CH₄-CO₂ and CO₂-N₂ fluid inclusions;
 modelling for T<31 degrees C and P<400 bars. Eur. J. Mineral. 6, 753–771.
 Thompson, A.B., Connolly, J.A.D., 1992. Migration of metamorphic fluid: some aspects of mass and
 heat transfer. Earth-Sci. Rev. 32, 107–121. [https://doi.org/10.1016/0012-8252\(92\)90014-K](https://doi.org/10.1016/0012-8252(92)90014-K)
 Touret, J.L.R., 2001. Fluids in metamorphic rocks. Lithos, Fluid Inclusions: Phase Relationships -
 Methods - Applications. A Special Issue in honour of Jacques Touret 55, 1–25.
[https://doi.org/10.1016/S0024-4937\(00\)00036-0](https://doi.org/10.1016/S0024-4937(00)00036-0)
 Van den Kerkhof, 1988. The system CO₂-CH₄-N₂ in fluid inclusions: theoretical modelling and
 geological applications.
 Van den Kerkhof, A., Thiéry, R., 2001. Carbonic inclusions. Lithos 55, 49–68.
 van den Kerkhof, A.M., 1990. Isochoric phase diagrams in the systems CO₂-CH₄ and CO₂-N₂:
 Application to fluid inclusions. Geochim. Cosmochim. Acta 54, 621–629.
[https://doi.org/10.1016/0016-7037\(90\)90358-R](https://doi.org/10.1016/0016-7037(90)90358-R)
 Wagner, W., Pruss, A., 1993. International Equations for the Saturation Properties of Ordinary Water
 Substance. Revised According to the International Temperature Scale of 1990. Addendum to
 J. Phys. Chem. Ref. Data 16, 893 (1987). J. Phys. Chem. Ref. Data 22, 783–787.
<https://doi.org/10.1063/1.555926>
 Wang, C.H., Wright, R.B., 1973. Effect of density on the Raman scattering of molecular fluids. I. A
 detailed study of the scattering polarization, intensity, frequency shift, and spectral shape in
 gaseous N₂. J. Chem. Phys. 59, 1706–1712. <https://doi.org/10.1063/1.1680252>
 Wang, W., Caumon, M.-C., Tarantola, A., Pironon, J., Lu, W., Huang, Y., 2019. Raman spectroscopic
 densimeter for pure CO₂ and CO₂-H₂O-NaCl fluid systems over a wide P-T range up to
 360 °C and 50 MPa. Chem. Geol. 528, 119281.
<https://doi.org/10.1016/j.chemgeo.2019.119281>
 Wang, X., Chou, I.-M., Hu, W., Burruss, R.C., Sun, Q., Song, Y., 2011. Raman spectroscopic
 measurements of CO₂ density: Experimental calibration with high-pressure optical cell
 (HPOC) and fused silica capillary capsule (FSCC) with application to fluid inclusion
 observations. Geochim. Cosmochim. Acta 75, 4080–4093.
<https://doi.org/10.1016/j.gca.2011.04.028>
 Wilkinson, J.J., 2001. Fluid inclusions in hydrothermal ore deposits. Lithos, Fluid Inclusions: Phase
 Relationships - Methods - Applications. A Special Issue in honour of Jacques Touret 55, 229–
 272. [https://doi.org/10.1016/S0024-4937\(00\)00047-5](https://doi.org/10.1016/S0024-4937(00)00047-5)

- Wopenka, B., Pasteris, J.D., 1986. Limitations to Quantitative Analysis of Fluid Inclusions in Geological Samples by Laser Raman Microprobe Spectroscopy. *Appl. Spectrosc.* 40, 144–151.
- Wright, R.B., Wang, C.H., 1973. Density effect on the Fermi resonance in gaseous CO₂ by Raman scattering. *J. Chem. Phys.* 58, 2893–2895. <https://doi.org/10.1063/1.1679594>
- Yamamoto, J., Kagi, H., 2006. Extended Micro-Raman Densimeter for CO₂ Applicable to Mantle-originated Fluid Inclusions. *Chem. Lett.* 35, 610–611. <https://doi.org/10.1246/cl.2006.610>
- Yamamoto, J., Kagi, H., Kaneoka, I., Lai, Y., Prikhod'ko, V.S., Arai, S., 2002. Fossil pressures of fluid inclusions in mantle xenoliths exhibiting rheology of mantle minerals: implications for the geobarometry of mantle minerals using micro-Raman spectroscopy. *Earth Planet. Sci. Lett.* 198, 511–519. [https://doi.org/10.1016/S0012-821X\(02\)00528-9](https://doi.org/10.1016/S0012-821X(02)00528-9)
- Yamamoto, J., Kagi, H., Kawakami, Y., Hirano, N., Nakamura, M., 2007. Paleo-Moho depth determined from the pressure of CO₂ fluid inclusions: Raman spectroscopic barometry of mantle- and crust-derived rocks. *Earth Planet. Sci. Lett.* 253, 369–377. <https://doi.org/10.1016/j.epsl.2006.10.038>
- Yuan, X., Mayanovic, R.A., Zheng, H., Sun, Q., 2017. Determination of pressure in aqueo-carbonic fluid inclusions at high temperatures from measured Raman frequency shifts of CO₂. *Am. Mineral.* 102, 404–411. <https://doi.org/10.2138/am-2017-5405>
- Zakin, M.R., Herschbach, D.R., 1986. Vibrational frequency shifts induced by molecular compression of pyridine in solution. *J. Chem. Phys.* 85, 2376–2383. <https://doi.org/10.1063/1.451092>
- Zhang, J., Qiao, S., Lu, W., Hu, Q., Chen, S., Liu, Y., 2016. An equation for determining methane densities in fluid inclusions with Raman shifts. *J. Geochem. Explor., Fluid and Melt inclusions* 171, 20–28. <https://doi.org/10.1016/j.gexplo.2015.12.003>